

Passive Detection, Characterization, and Localization of Multiple LFMCW LPI Signals ^{*†‡}

Brandon Hamschin^a, John Clancy ^a, Mike Grabbe ^a, Matthew Fortier ^a, John Novak^b

^aThe Johns Hopkins University, Applied Physics Laboratory, Laurel, Maryland 20723

^b ASD (R&E)/RD/Space and Sensor Systems, Alexandria, Virginia 2235

ABSTRACT

A method for passive Detection, Characterization, and Localization (DCL) of multiple low power, Linear Frequency Modulated Continuous Wave (LFMCW) (*i.e.*, Low Probability of Intercept (LPI)) signals is proposed. In contrast to other detection and characterization approaches, such as those based on the Wigner-Ville Transform (WVT)¹ or the Wigner-Ville Hough Transform (WVHT),² our approach does not begin with a parametric model of the received signal that is specified directly in terms of its LFMCW constituents. Rather, we analyze the signal over time intervals that are short, non-overlapping, and contiguous by modeling it within these intervals as a sum of sinusoidal (*i.e.*, harmonic) components with unknown frequencies, deterministic but unknown amplitudes, unknown order (*i.e.*, number of harmonic components), and unknown noise autocorrelation function. Using this model of the signal, which we refer to as the Short-Time Harmonic Model (STHM), we implement a detection statistic based on Thompson's Method for harmonic analysis,³ which leads to a detection threshold that is a function of False Alarm Probability P_{FA} and not a function of the noise properties. By doing so we reliably detect the presence of *multiple* LFMCW signals in colored noise without the need for prewhitening, efficiently estimate (*i.e.*, characterize) their parameters, provide estimation error variances for a subset of these parameters, and produce Time-of-Arrival (TOA) estimates that can be used to estimate the geographical location of (*i.e.*, localize) each LFMCW source. Finally, by using the entire time-series we refine these parameter estimates by using them as initial conditions to the Maximum Likelihood Estimator (MLE), which was originally given in¹ and later found in² to be too computationally expensive for multiple LFMCW signals if accurate initial conditions were not available to limit the search space. We demonstrate the performance of our approach via simulation.

Keywords: Detection, Low Probability of Intercept, Linear Frequency Modulated Continuous Wave, Geolocation, Multitaper Methods

1. INTRODUCTION

The development of radar systems that employ low power waveforms with long duration and large bandwidths were, in part, born out of the advent and proliferation of solid-state amplifier technology.⁴ This technology enabled the production of small, lightweight radar systems that are capable of reliable detection (due to the signal's long duration), and precise ranging (due to the signal's wide bandwidth) at moderate standoff ranges. In many maritime environments, these radar systems are not only attractive from a size, cost, and performance standpoint, but also because of their potential to operate covertly in the presence of legacy Electronic INTelligence (ELINT) systems, which are simply not equipped to handle low power, long duration, wide band signals. Consequently, they are replacing many of the high-power, pulsed Continuous Wave (CW) radars of the past.

While numerous practical approaches exist for Detecting, Characterizing, and Localizing (DCL) legacy radar systems,⁵ relatively few exist for modern radar systems employing low-power Linear Frequency Modulated Continuous Wave (LFMCW) signals, in spite of their popularity [4, Ch. 2]. For this reason low power LFMCW signals are examples of radar waveforms that have become known as Low Probability of Intercept (LPI) signals. In [4, pgs. 3,4] Pace defines LPI and Low Probability of Identification (LPID) as follows:

DEFINITION 1. *A low probability of intercept (LPI) radar is defined as a radar that uses a special emitted waveform intended to prevent a non-cooperative intercept receiver from intercepting and detecting its emission.*

Portions of this research were presented at the 2014 IEEE Radar Conference in Cincinnati, OH.

This work was funded by the U.S. Department of Defense Office of the Assistant Secretary of Defense, Space and Sensor Systems.

Distribution Statement A: Approved for Public Release; Distribution is Unlimited

DEFINITION 2. *Low probability of identification (LPI) radar is defined as a radar that uses a special emitted waveform intended to prevent a non-cooperative intercept receiver from intercepting and detecting its emission but if intercepted, makes identification of the emitted waveform modulation and its parameters difficult.* In [5, pg. 211] Wiley defines an LPI radar as:

DEFINITION 3. *...a radar system whose signal is below the level of threshold of detection of opposing ELINT receivers while still being able to detect targets at useful ranges.*

The common thread between both Pace's and Wiley's definitions of LPI and LPID[§] radar is that the non-cooperative (*i.e.*, passive) intercept receiver in question is ill-suited to collect ELINT for the waveform employed. Given that the majority of commercial and military grade radars operate using high peak power, short duration, pulsed CW signals and, therefore, most ELINT systems have been designed for those threats, a case can be made that modern signals are considered LPI because legacy ELINT receivers are being used to judge their interceptability and identifiability. In other words, attempts to use legacy ELINT receivers to detect and identify these new threats yields results that have a *Low Probability* of success. Hence, new algorithms for collecting ELINT on these new waveforms are needed so that the probability of intercepting these new waveforms is no longer low.

1.1 Background

Whether they are designed for legacy or modern radar waveforms, passive detection and characterization approaches can be broken into two categories: Noncoherent and Coherent.

1.1.1 Noncoherent Approaches

Noncoherent approaches remove signal phase information during processing, usually by considering only the magnitude of the signal, thus simplifying the processing and making them well suited for high power, pulsed CW legacy threats. Some examples of noncoherent detection are integrated energy detectors and M of N detectors, [5, pg. 212-226], [6, Ch. 6], and.⁷ In practice, both of these approaches requires one to assume that the noise is white and its power level is known and constant [6, pg. 347] over the collection duration in order to set a threshold that relates to the Probability of False Alarm (P_{FA}). Another approach, known as Constant False Alarm Rate (CFAR) detection [6, pgs. 347-382], does not require that the noise power is known or constant, but does require that it is white and Gaussian for P_{FA} based threshold selection. A vice and virtue of all noncoherent approaches is that they operate using detection statistics that are functions of energy alone, which makes them independent of any potential phase modulation. This is a virtue because one does not need to assume anything about the structure of the transmitted signals, making the resulting approaches very general and well suited for the high-power legacy CW threats that typically contain no intentional phase modulation. The downside to this, which is especially pronounced when attempting to collect ELINT on LFMCW signals, is that in the absence of further processing one cannot ascertain information such as chirp-rate, modulation period, or bandwidth since these parameters are embedded in the phase.

1.1.2 Coherent Approaches

Coherent, in contrast to noncoherent approaches, use signal phase during processing. Since most systems using sophisticated modulation schemes to make themselves LPI are based on Linear Frequency Modulation (LFM) [4, Ch. 1,2, and 4] [5, pg. 226], the most popular of the coherent approaches for LPI ELINT are based on the Wigner-Ville Transform (WVT). From a purely Time-Frequency Analysis (TFA) viewpoint, the prominence of the WVT is owed to the fact that for a single LFM chirp the Wigner-Ville Distribution (WVD) is completely concentrated along the signal's instantaneous frequency [8, pg. 121], which is defined by a single straight line, and characterized by its slope ($a/k/a$ chirp-rate) β and frequency intercept f^{int} . The feature of the WVT makes it an attractive starting point for image processing techniques that are designed to detect edges or lines, such as the Radon or Hough Transforms.

[§]For the remainder of this paper we refer to the low-power, long-duration, LFMCW signals that we focus on as LPI, rather than, say, LPID.

From a detection and estimation theory viewpoint, the use of the WVD was first motivated by,¹ wherein the Generalized Likelihood Ratio Test (GLRT) [7, pgs. 187-189] was derived to decide between the following hypotheses

$$\mathcal{H}_0 : \tilde{r}(t) = \tilde{w}(t) \quad (1)$$

$$\mathcal{H}_1 : \tilde{r}(t) = \tilde{b} \cdot \tilde{s}(t; \bar{\theta}) + \tilde{w}(t) \quad (2)$$

where $\tilde{s}(t; \bar{\theta})$ is the complex representation of the transmitted signal, $\tilde{r}(t)$ is the noisy received signal, and $\tilde{b} = b_R + jb_I$ is a zero mean complex Gaussian random variable with variance $\sigma_{\tilde{b}}^2$ that models the signal amplitude. Furthermore, b_R and b_I are assumed to be mutually uncorrelated real Gaussian random variables with zero mean and equal variances $\sigma_{b_R}^2 = \sigma_{b_I}^2 = \sigma_b^2/2$. Additionally, $\tilde{w}(t)$ is band-limited, zero mean, complex white Gaussian noise with $\tilde{w}(t) = w_R(t) + jw_I(t)$, where $w_R(t)$ and $w_I(t)$ are each assumed to be zero mean white Gaussian noise processes independent of each other and with the identical Power Spectral Densities (PSD). Hence $w_R(t) \sim \mathcal{N}(0, \sigma_w^2/2)$, $w_I(t) \sim \mathcal{N}(0, \sigma_w^2/2)$, $E\{w_R(t_1)w_I(t_2)\} = 0 \forall t_1, t_2 \in [0, T]$, where T is the observation duration and the PSD of $\tilde{w}(t)$ is $P_{\tilde{w}}(f) = \sigma_{\tilde{w}}^2$. In general, the GLRT was found to be the maximum of the magnitude-squared of the 1-D correlation between the received signal $\tilde{r}(t)$ and all possible templates of the transmitted signal $\tilde{s}(t; \bar{\theta})$. More specifically, the GLRT was shown to decide \mathcal{H}_1 if

$$\mathcal{L} = \max_{\bar{\theta}} \left| \int_0^T \tilde{r}(t) \tilde{s}^*(t; \bar{\theta}) dt \right|^2 > \eta \quad (3)$$

The Maximum Likelihood Estimate (MLE) of $\bar{\theta}$, denoted by $\hat{\theta}$, is the value of $\bar{\theta}$ that maximizes Equation (3) when the threshold η is exceeded. Unfortunately, while optimal in the GLRT sense, no guidance is given for selecting η , which implies no control over P_{FA} . In other words, when the signal is actually present the detector will likely do a very good job at indicating such, but when the signal is not present false detections are beyond the designers control.

The WVD was brought into the solution found in¹ by invoking Moyal's formula [8, pgs. 128-129] to show that 1-D correlation in Equation (3) is equivalent to a 2-D correlation between the WVD of the received signal $\mathcal{W}_{\tilde{r}}(t, \omega)$ and the WVD of $\tilde{s}(t; \bar{\theta})$, denoted by $\mathcal{W}_{\tilde{s}}(t, \omega; \bar{\theta})$. Specifically,

$$\left| \int_0^T \tilde{r}(t) \tilde{s}^*(t; \bar{\theta}) dt \right|^2 = \int_{-\infty}^{\infty} \int_{-\infty}^{\infty} \mathcal{W}_{\tilde{r}}(t, \omega) \mathcal{W}_{\tilde{s}}(t, \omega; \bar{\theta}) dt \frac{d\omega}{2\pi} \quad (4)$$

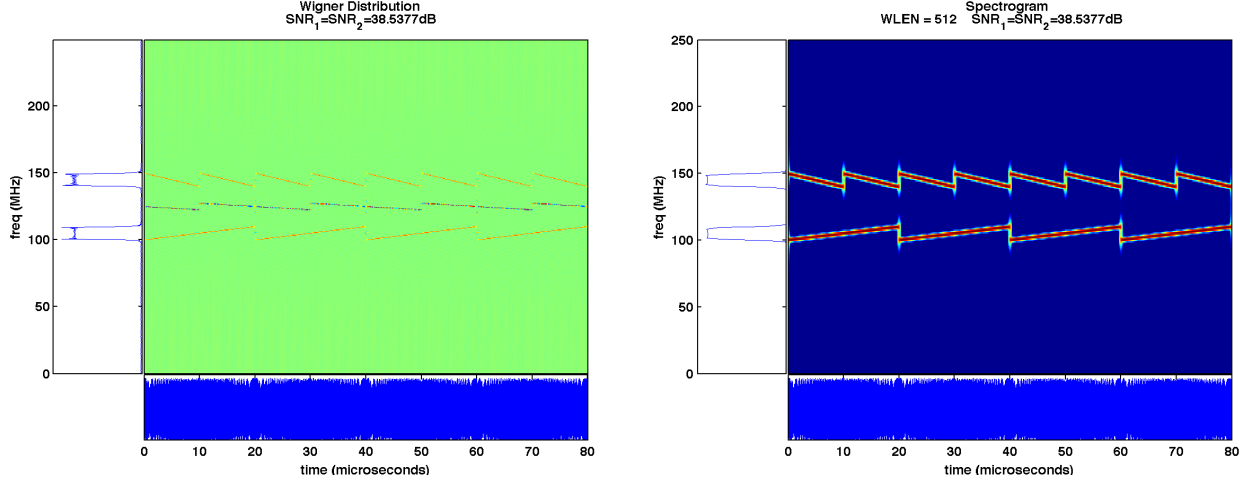
If $\tilde{s}(t)$ is assumed to be a single LFM chirp, defined by $\tilde{s}(t; \bar{\theta}) = e^{j(2\pi f^{\text{int}} t + \pi \beta t^2)}$, where $\bar{\theta} = [f^{\text{int}} \quad \beta]^T$, then $\mathcal{W}_{\tilde{s}}(t, \omega; \bar{\theta})$ reduces to

$$\mathcal{W}_{\tilde{s}}(t, \omega; \bar{\theta}) = 2\pi\delta(\omega - 2\pi f^{\text{int}} - 2\pi\beta t) \quad (5)$$

where $\delta(\cdot)$ is the Dirac Delta function. Substituting (4) and (5) into (3) yields

$$\mathcal{L} = \max_{f^{\text{int}}, \beta} \int_{-\infty}^{\infty} \mathcal{W}_{\tilde{r}}(t, 2\pi f^{\text{int}} + 2\pi\beta t) dt > \eta \quad (6)$$

Hence the GLRT for a single LFM chirp is equivalent to path integration of the WVD along paths determined by different chirp-rates and frequency intercepts. If the value of any such path integral, which is equivalent to a point in the Hough or Radon Transform domain of the WVD, exceeds the detection threshold η then a single LFM signal is detected with the MLE of its parameters being the \hat{f}^{int} and $\hat{\beta}$ that defined the maximum path integral that exceeded the threshold. Unfortunately, even for this special case, no direction on how to select η was given, which suggests one's only recourse is to either assume a PDF for $\tilde{r}(t)$ under \mathcal{H}_0 , estimate it with built-in testing equipment, or estimate it off-line with laboratory experiments. Each of these options is potentially costly and error prone but seem to be common in practice given the absence of any alternatives in the literature.



(a) WVD of two LFMCW signals (main panel) Frequency (b) Spectrogram (40 dB dynamic range) of two LFMCW signals (main panel) Frequency marginal of WVD (left panel) Time-series $r(t)$ (bottom panel) Frequency marginal of spectrogram (left panel) Time-series $r(t)$ (bottom panel)

Figure 1: Time-frequency distributions of $r(t)$ containing two LFMCW signals based on signal model given in Equation (9) from²

In² the authors show that if one assumes the signal of interest (SOI) is the sum of multiple LFMCW signals with deterministic but unknown amplitudes, the resulting GLRT is equivalent to that derived in¹ and given above in Equation (3). Their model for the received signal under \mathcal{H}_0 is the same as in¹ but \mathcal{H}_1 becomes

$$\mathcal{H}_1 : \tilde{r}(t) = \tilde{s}(t; \bar{\theta}) + \tilde{w}(t) \quad (7)$$

where

$$\tilde{s}(t; \bar{\theta}) = \sum_{m=1}^M \tilde{s}_m(t; \bar{\theta}_m) \quad (8)$$

$$\tilde{s}_m(t; \bar{\theta}_m) = b_m e^{j(\varphi_m + 2\pi f_m^{\text{start}} t + \pi \beta_m \bmod (t + \Delta_m, T_{p,m}))^2} \quad (9)$$

$$\bar{\theta} = [\bar{\theta}_1^T \dots \bar{\theta}_M^T]^T \quad (10)$$

$$\bar{\theta}_m = [\varphi_m \ f_m^{\text{start}} \ \beta_m \ \Delta_m \ T_{p,m}]^T \quad (11)$$

Figures 1a and 1b show the WVD and spectrogram, respectively, of a high SNR received signal containing two LFMCW components that adhere to the signal model used in² and summarized in Equations (7)-(11). The signal is observed over the time-interval $0 \leq t \leq T = 80 \ \mu s$ and sampled at $F_S = \frac{1}{T_s} = 500 \text{ MHz}$. For the purposes of this paper we define SNR of the m^{th} LFMCW signal as

$$\text{SNR}_m = \frac{b_m^2}{2\sigma_w^2} \quad (12)$$

and b_m and ϕ_m are treated as nuisance parameters. The remaining signal properties for this example are summarized in Table 1.

While high SNR at the output of a GLRT detector is desirable since it yields high Probability of Detection (P_D), its practicality is limited when the detection statistic admits no systematic method for determining η . Furthermore, the authors of² make it clear that implementing their detector for the case when $M > 1$ is impractical due to the computational burden that results. Moreover, even if their approach were computationally feasible, the authors give no systematic and efficient way of determining M . Finally, careful consideration of Equation (9) reveals that their signal model forces the entire observation interval to be occupied by LFMCW

energy, which is a limitation for two reasons. First, a passive receiver cannot control when the emitter begins to transmit relative to when the receiver begins to record. A way around this might be to limit $\tilde{r}(t)$ so that it adheres to Equation (9), but such a procedure runs the risk of losing valuable signal information, such as Time of Arrival (TOA). Second, without a parameter that models delay relative to $t = 0$, the TOA of each signal may be unobservable. Without the capacity to estimate TOA, multi-platform geo-location based on TOA differences is impossible.

Table 1: Signal Parameters for Figure 1

Variable Description	Variable Name	Values (m=1, m=2)	Units
No. of LFMCW Signals	M	2	—
Amplitude	b_m	1,1	$\sqrt{J/s}$
Phase	φ_m	0,0	rad
Starting Frequency	f_m^{start}	100,150	MHz
Chirp-Rate	β_m	0.5,-1.0	MHz
Time-Offset	Δ_m	0,0	μs
Modulation Period	$T_{p,m}$	20,10	μs

1.2 Overview of This Work

In contrast to other coherent approaches to detecting and characterizing LFMCW signals,^{1,2} our approach analyzes the received time-series over short, non-overlapping, contiguous time intervals, which is an approach that is motivated by the numerous window based methods that are commonplace in *spectral analysis*.^{3,9} Within each interval the received signal is modeled as a sum of harmonic components with unknown order and, within this interval, zero or more frequency components are detected and estimated. Over time these estimates are collected and used to produce final estimates of each parameter in our new model of the received signal, which is close to that given in Equations (7)-(11), but differs in several important ways. First, we model the data as being real-valued[¶], which is indicated by the omission of a tilde over the variables. Second, we include two temporal parameters that allow for the specification of both TOA, τ_m , and stop-time, t_m^{stop} . Third, the only assumption made on $w(t)$ is that its PDF is Gaussian for each t . In other words, the autocorrelation function of $w(t)$ need not be known, thereby eliminating the need to prewhitening $r(t)$ if $w(t)$ is colored. Fourth, and finally, we assume that the initial phase φ_m does not significantly impact the value of the other parameter estimates and assume it to be zero. Hence, Equations (7)-(11) become

$$\mathcal{H}_1 : r(t) = s(t; \bar{\theta}) + w(t) \quad (13)$$

where

$$s(t; \bar{\theta}) = \sum_{m=1}^M s_m(t; \bar{\theta}_m) \quad (14)$$

$$s_m(t; \bar{\theta}_m) = b_m \cos \left(2\pi f_m t + \pi \beta_m \bmod (t + \Delta_m, T_{p,m})^2 \right) \times \\ (u(t - \tau_m) - u(t - t_m^{\text{stop}})) \quad (15)$$

$$\bar{\theta} = [\bar{\theta}_1^T \dots \bar{\theta}_M^T]^T \quad (16)$$

and the unknown parameter vector is modified to include τ_m and t_m^{stop}

$$\bar{\theta}_m = [b_m \quad \tau_m \quad t_m^{\text{stop}} \quad f_m^{\text{start}} \quad \beta_m \quad \Delta_m \quad T_{p,m}]^T \quad (17)$$

The spectrogram of an example received signal adhering to the data model given in Equations (14)-(17) is given in Figure 2, with associated parameters summarized in Table 2. This example signal is used throughout the paper to highlight various aspects of the DCL process.

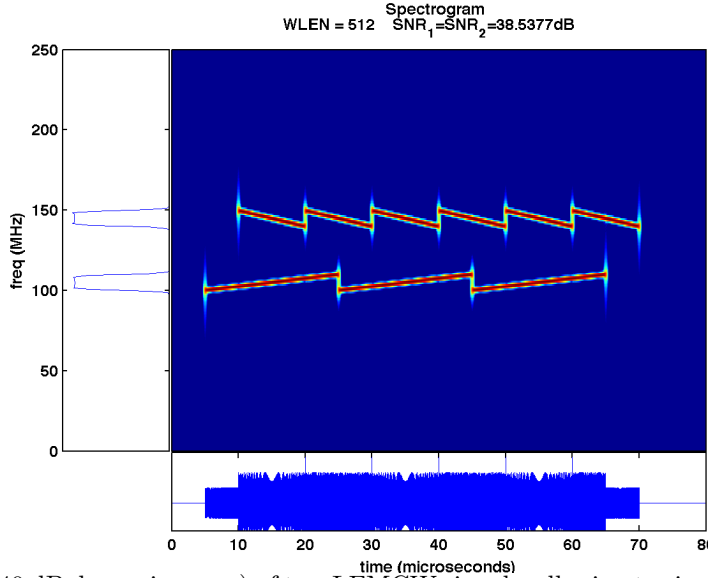


Figure 2: Spectrogram (40 dB dynamic range) of two LFMCW signals adhering to signal model given in Equation (15) (main panel) frequency marginal of spectrogram (left panel) Time-series $r(t)$ (bottom panel)

Table 2: Signal Parameters for Figure 2

Variable Description	Variable Name	Values (m=1, m=2)	Units
No. of LFMCW Signals	M	2	N/A
Initial Frequency	f_m	100,150	MHz
Chirp-Rate	β_m	0.5,-1.0	MHz
Time-Offset	Δ_m	15,0	μs
Modulation Period	$T_{p,m}$	20,10	μs
Time-of-Arrival	τ_m	5,10	μs
Stop Time	$t_{stop,m}$	65,70	μs

To summarize, the most salient features of our work that are absent from any single approach in the literature are: (1) no calibration is necessary, either in-situ or in the laboratory, to determine detection threshold η settings as a function of P_{FA} ; (2) one does **not** need to assume the system noise present in the received time-series is white or has a known autocorrelation function, thereby eliminating the potential need for prewhitening $r(t)$; (3) environments containing multiple LFMCW signals can be treated without adding a stifling computational burden; (4) direct recognition of the number of LFMCW signals in the environment is achieved; (5) in addition to estimates of the parameters that define the instantaneous frequency of each LFMCW signal, our approach produces estimates of the variance of a subset of these parameters directly from the data; (6) estimates of the TOA of each LFMCW signal are obtained, which can be used to localize each LFMCW source if three or more stationary ELINT receivers are present, or if two or more moving receivers are available with synchronized clocks.

The remainder of this paper is devoted to developing our approach and analyzing its performance. To do so it is organized as follows. Sections 2-4 cover the algorithmic details associated with each part of the DCL process. In particular, the detection algorithms are detailed in Section 2, the characterization algorithms in Section 3, and the localization algorithms in Section 4. The mathematical details contained in each of these sections are reinforced by a simulation example that is based on the signal first introduced in Figure 2 and Table 2. For the examples found in Sections 2 and 3, noise is added to the true signal so that a moderate level of SNR, which is defined in Equation (12), is achieved with $b_1 = b_2 = 1$. In Section 4, noise is added to each received signal

*The modifications to the theory necessary to extend the model to complex data are straightforward, but not discussed in this paper.

based on the SNR predicted by a link-budget analysis [10, pgs. 66-84]. The reason this more detailed method for computing SNR is employed is so that we can incorporate transmitter power levels that are consistent with our assumption that the transmitted signals are LPI. Specifically, we assume each LPI radar operates at an Effective Isotropically Radiated Power (EIRP) of 1 Watt and a carrier frequency of 10 GHz. Moreover, we assume each of the three ELINT receivers has an effective noise bandwidth of 50 MHz, a noise figure of 6 dB, and an antenna gain of 10dB. By demonstrating results under these detailed modeling conditions we provide evidence that there is enough power in a narrow window of time required for the Short-Time Harmonic Model (STHM) to prosecute real-world signals using real-world receivers. In Section 5 we show characterization performance as a function of SNR based on a Monte Carlo simulation and show localization performance using a deterministic approach as a function of range and TOA variance. Finally, in Section 6 we highlight the main features of the this work, potential downsides, and suggest future directions.

2. DETECTION

In this section we describe the *detection* stage of the algorithm. We use the term 'detection' to refer to this step since it is where we formulate the first hypothesis test. To clarify what we mean by a detection consider the following hypothesis test ^{||}

$$\mathcal{H}_0 : r_{n,k} = w_{n,k} \quad (18)$$

$$\mathcal{H}_1 : r_{n,k} = s_{n,k} + w_{n,k} \quad (19)$$

where $r_{n,k}$ is the n^{th} sample, for $n = 1, \dots, N$, of $r(t)$ in the k^{th} time interval. The k^{th} time interval is given by $\delta_k = \{t : (k-1)(N-1)T_s \leq t \leq k(N-1)T_s\}$ where $k = 1, \dots, K = \lfloor \frac{T}{N \cdot T_s} \rfloor$. In other words, $r_{n,k} = r((k-1)(N-1)T_s + (n-1)T_s)$. Within this short time interval we model the received time-series as a sum of harmonic components, which gives rise to the following Short Time Harmonic Model (STHM) of the data

$$s_{n,k} \approx s_{n,k}^{\text{STHM}} = \sum_{c=1}^{L_k} A_{c,k} \cdot \cos(2\pi f_{c,k} n T_s + \phi_{c,k}) \quad (20)$$

where L_k is the number of constant frequencies $f_{c,k}$ present in δ_k , with $b_{c,k}$ and $\phi_{c,k}$ being the associated amplitudes and phases, respectively. We emphasize that L_k and each $b_{c,k}$, $f_{c,k}$, and $\phi_{c,k}$ are assumed to be unknown, but deterministic. From this point forward we take the approximation in Equation (20) to be an equality. Furthermore, in δ_k we assume that $w_{n,k}$ is a band-limited, zero mean, Gaussian random process with unknown PSD, $P_{w_{n,k}}(f)$, that is not necessarily constant (*i.e.*, $\{w_{n,k}\}$ can be colored noise), but is slowly-varying. The ability to handle an unknown colored noise process is what justifies Item 2 from Subsection 1.2. Thus, the STHM of the received multicomponent LFMCW signal in δ_k is

$$r_{n,k} = s_{n,k}^{\text{STHM}} + w_{n,k} \quad (21)$$

Hence, within δ_k selection between \mathcal{H}_0 and \mathcal{H}_1 can be achieved using Thompson's multi-taper based method for harmonic analysis, which was first proposed in¹¹ and later summarized in [3, pgs. 331-374, 496-514]. In what follows we overview the method by following [3, pgs. 331-374, 496-514] closely and highlighting its main features in the context of our LPI DCL problem.

2.1 Steps for Detecting and Estimating STHM Parameters via Thompson's Method

Under \mathcal{H}_1 , $\{r_{n,k}\}$ is a set of samples with a sinusoidally varying mean. Accordingly, the goal of the decision procedure in Equations (18) and (19) is to determine whether the mean is statistically different from zero and consistent with the harmonic model of the mean given in Equation (20). The key idea behind making this determination is to express Equation (21) in the frequency domain and, upon application of Thompson's multi-taper method, recognize the regression problem that results. The decision procedure then amounts to determining the statistical significance of the computed regression coefficients, which leads to estimates of $b_{c,k}$, $f_{c,k}$ and, $\phi_{c,k}$.

^{||}We reference the samples of a continuous time signal $x(t)$ as $x_n \equiv x(t)|_{t=nT_s}$

For the sake of brevity the detailed development of Thompson's method is omitted from this paper, but the reader can consult [3, pgs. 331-374, 496-514] for an excellent description of the method for harmonic analysis.

We now give a summary of the steps necessary to test whether the samples in δ_k contain significant frequencies, determine estimates of their values, and compute estimates of L_k , $A_{c,k}$, $f_{c,k}$ and $\phi_{c,k}$.

Step 0 – For even $q \in \{0 \dots Q - 1\}$, with $Q = 2NW - 1$, compute the associated length N DPSS data taper $\{h_{q,n}\}$ [3, Ch. 8] where N is the number of samples taken in δ_k at the sample rate F_s . The resolution bandwidth W , for W in the normalized frequency range $0 \leq W \leq 0.5$, determines the minimum separation between frequencies in the same δ_k that can be resolved. In other words, distinct frequencies $f_{1,k}$ and $f_{2,k}$ will be indistinguishable if $|f_{1,k} - f_{2,k}| / F_s < 2W$. Assuming N and W are fixed for all δ_k , this step only needs to be performed once and the tapers applied to each δ_k .

Step 1 – For $p = 0, \dots, N_{FFT}/2 - 1$, compute samples of $J_{q,k}(f)$ using an N_{FFT} point Fast Fourier Transform (FFT). Specifically, let $J_{q,k}(p \cdot \Delta f)$, where $\Delta f \equiv F_s/N_{FFT}$, be the p^{th} point of the FFT of $\{\sqrt{T_s} \cdot h_{q,n} \cdot r_{n,k}\}$.

Step 2 – For $q \in \{0, \dots, Q - 1\}$, compute $H_q(0) = T_s \sum_{n=1}^N h_{q,n}$

Step 3 – For $p = 0, \dots, N_{FFT}/2 - 1$, compute $C(p \cdot \Delta f) \equiv \sqrt{T_s} \cdot \frac{\sum_{q=0}^{Q-1} J_{q,k}(p \cdot \Delta f) H_q(0)}{\sum_{q=0}^{Q-1} H_q^2(0)}$

Step 4 – For each $q \in \{0, \dots, Q - 1\}$ and each $p = 0, \dots, N_{FFT}/2 - 1$, compute $\hat{J}_{q,k}(p \cdot \Delta f) \equiv C(p \cdot \Delta f) \frac{H_q(0)}{\sqrt{T_s}}$

Step 5 – For $p = 0, \dots, N_{FFT}/2 - 1$, compute $D_k(p \cdot \Delta f) = \frac{(Q-1)|C(p \cdot \Delta f)|^2 \sum_{q=0}^{Q-1} H_q^2(0)}{T_s \sum_{q=0}^{Q-1} |J_{q,k}(p \cdot \Delta f) - \hat{J}_{q,k}(p \cdot \Delta f)|^2}$

Step 6 – For a given P_{FA} , compute the detection threshold η by $\eta = \frac{(Q-1)(1-P_{FA})^{1/(Q-1)}}{P_{FA}^{1/(Q-1)}}$, since under \mathcal{H}_0 , $D_k(p \cdot \Delta f) \sim F_{2,2Q-2}$ [3, pg. 501]

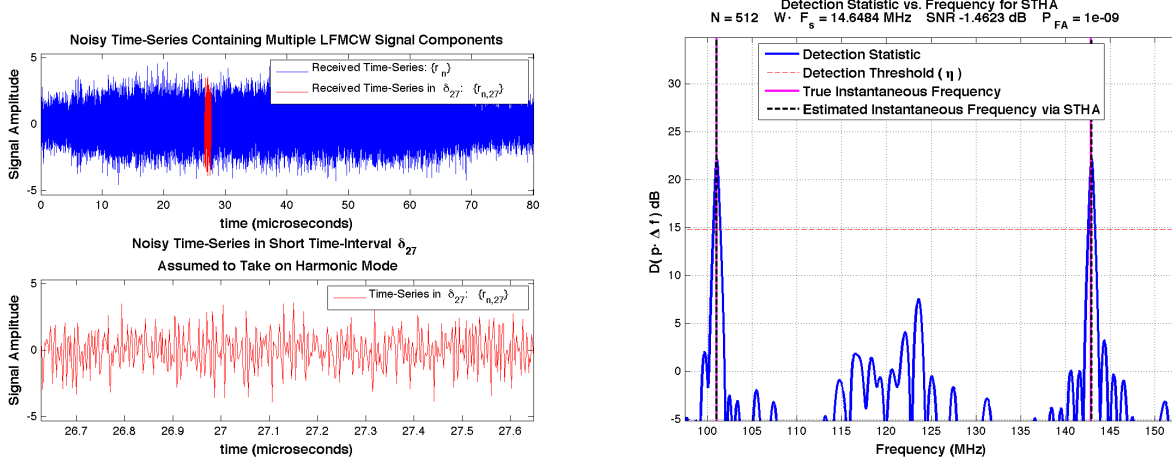
Step 7 – Select the indices, denoted by p_c , corresponding to the largest values of $\{D_{p,k}\}$ such that $D_k(p \cdot \Delta f) \geq \eta$ and $|p_i - p_j| > \left\lceil \frac{W \cdot F_s}{\Delta f} \right\rceil$. The number of peaks meeting these criterion is the estimate of L_k , with associated frequency estimates given by $\hat{f}_{c,k} = p_c \Delta f$. Amplitude and phase estimates are given by $\hat{b}_{c,k} = |\hat{C}_{c,k}|$ and $\hat{\phi}_{c,k} = 2 \cdot \tan^{-1} \left(\frac{\text{Im}\{\hat{C}_{c,k}\}}{\text{Re}\{\hat{C}_{c,k}\}} \right)$, respectively.

Following Step 6 we have a (potentially empty) set of ordered pairs $\mathcal{S}_k = \left\{ \left(t_k, \hat{f}_{1,k} \right), \dots, \left(t_k, \hat{f}_{L_k,k} \right) \right\}$ corresponding to frequency estimates made at time t_k , where t_k is defined to be the sample time closest to the center of δ_k . Implementing this sequence of steps for all k produces the set $\mathcal{S} = \{\mathcal{S}_1, \dots, \mathcal{S}_K\}$ containing all frequency estimates obtained in the time interval $(0, T)$. The set \mathcal{S} is the main input to the Characterization step, which is described in Section 3.

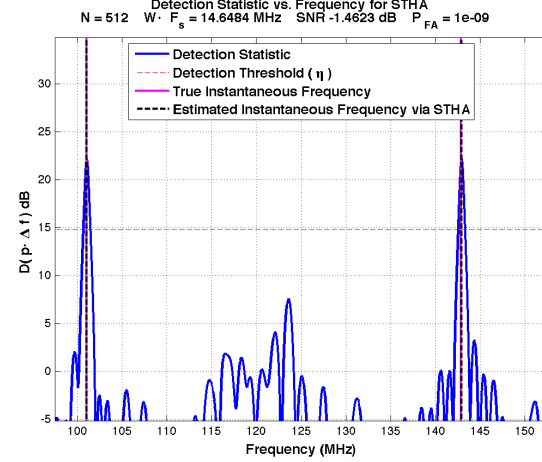
If no significant frequency components exist in any of time intervals δ_k then the DCL process is terminates and declares no LFMCW signals are present in the environment.

2.2 Detection Example

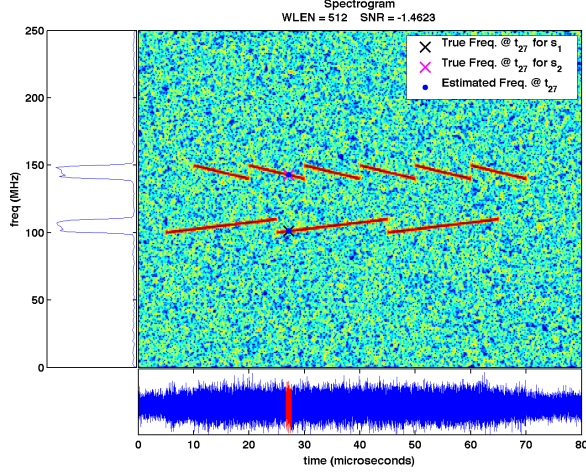
In the remainder of this section we give an example of detection based on the STHM. The signal used is identical to that given in Figure 2 and Table 2 except that noise is added so that $\text{SNR}_1 = \text{SNR}_2 = -1.4632$ dB. The top panel of Figure 3a shows the whole time-series $\{r_n\}$ in blue and $\{r_{n,27}\}$ overlaid in red. A closer look at $\{r_{n,27}\}$, which we assume adheres to the STHM given in Equation (20), is shown in the lower panel. Figure 3b shows the detection statistic that results from Steps 0-5, plotted as a function of frequency. To implement these



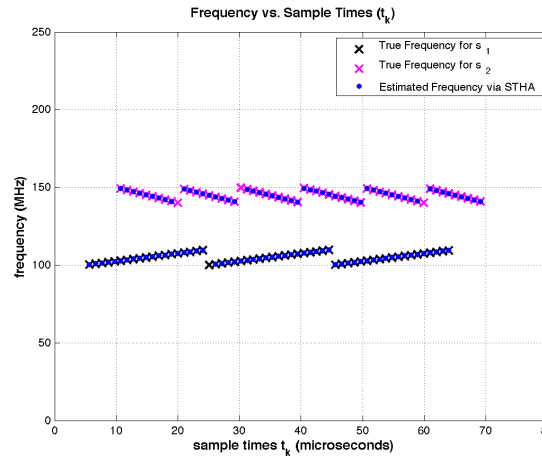
(a) Received Time-Series $\{r_n\}$ (Blue) and Received Time-Series in δ_{27} (Red)



(b) Detection Test Statistic Computed based Steps 0-6 using $\{r_{n,27}\}$



(c) Spectrogram (40 dB dynamic range) of $\{r_n\}$ with Frequency Estimates via STHA in δ_{27} (main panel) Frequency Marginal of the Spectrogram (left panel) Time-Series $\{r_n\}$ (lower panel)



(d) Frequency Estimates vs. Sample Time t_k

Figure 3: Detection Example

steps, and arrive at Figure 3b, we used $N_{FFT} = 8192$, $N = 512$, and $WF_s = 14.6485$ MHz, which resulted in the use of $Q = 2NW - 1 = 29$ data tapers. For $P_{FA} = 10^{-9}$ we set the threshold according to Step 6 and, following the execution of Step 6, we arrive at the following set of frequency estimates for δ_{27} and $t_{27} = 27.136 \mu_s$, $\mathcal{S}_{27} = \{(27.136 \mu_s, 101.074 \text{ MHz}), (27.136 \mu_s, 142.822 \text{ MHz})\}$ which are plotted, along with truth at t_{27} on the spectrogram given in the main panel of Figure 3c. For comparison, the true instantaneous frequency at t_{27} for $s_1(t; \bar{\theta}_1)$ is 101.068 MHz and 142.864 MHz for $s_2(t; \bar{\theta}_2)$.

Performing Steps 0-6 for each k yields the set \mathcal{S} , which is plotted in Figure 3d, along with truth. A close look at Figure 3d reveals two interesting things. First, estimates associated with the instantaneous frequency of each LFM CW signal appear to be very close to their true instantaneous frequencies. While visual confirmation is satisfying, any firm conclusion on the estimation accuracy is deferred to Section 5, wherein we determine how well these frequency estimates enable the estimation of each $\bar{\theta}_m$. Second, at the beginning and end of some chirp-segments (*e.g.*, the low frequency portion of the first chirp-segment associated with s_2) we see that there are missing frequency estimates. The missing frequency estimates are due to the fact that the associated δ_k did

not contain sufficient sinusoidal content since it was in the edge of a chirp-segment. This effect illuminates the trade-off between the size of N and detection performance. In particular, N should be chosen large enough so that enough sinusoidal content is present to produce a detection and small enough to obtain enough frequency estimates to sufficiently characterize the instantaneous frequency of each LFMCW signal. Additionally, N should not be chosen to be so large that within a δ_k the frequency has enough time increase or decrease. It should be clear that selection of an appropriate N requires some engineering judgment and perhaps some prior knowledge on the maximum and minimum expected chirp-rates.

The set \mathcal{S} is the main input to the Characterization step, which is described in Section 3.

3. CHARACTERIZATION

The characterization stage picks up where the detection stage leaves off by operating on \mathcal{S} . The purpose of this step is to produce estimates of $\hat{\theta}_m$ given by the signal model that accompanies Equation (17). The process by which these estimates are obtained is broken into 3 stages: (1) *Clustering*, wherein the frequency samples in \mathcal{S} are clustered by chirp segment; (2) *Association*, wherein the chirp-segments, and their associated frequency estimates, are associated to individual LFMCW signals; and (3) *Estimation*, wherein the estimates of all unknowns specified in Equations (15) and (17) are computed for each LFMCW signal.

3.1 Clustering

The core ideas associated with this stage are drawn from the clustering method proposed in,^{12,13} wherein the authors seek to estimate the locations of an unknown number of Radio Frequency (RF) sources using Line-of-Bearing (LOB) measurements by clustering the measurements into groups using a Mahalanobis distance criterion. Among the potentially numerous candidate clusters that arise due to one RF source, the optimal cluster is chosen to be the one that maximizes a likelihood function. Once the LOB measurements associated with the Maximum Likelihood (ML) cluster are determined, they are removed from the overall list of LOB measurements and the process is repeated until no feasible clusters are generated. For the purposes of our work the frequency estimates in \mathcal{S} are analogous to the LOB measurements and the chirp segments are analogous to RF source locations.

As in,^{12,13} we assume the number of chirp segments present in \mathcal{S} is unknown *a-priori* and we assume the frequency estimates can be modeled as $\hat{f}_{c,k} = f_{c,k}(\mathbf{x}_{c,k}) + \zeta_{f_{c,k}}$, where $f_{c,k}(\mathbf{x}_{c,k})$ is the true instantaneous frequency and $\mathbf{x}_{c,k} = [f_{c,k}^{\text{int}} \ \beta_{c,k}]^T$ is the vector of unknown parameters of the c^{th} chirp-segment in time interval δ_k corresponding to measurement time t_k . Hence $\hat{f}_{c,k}$ is now be interpreted as a measurement of the instantaneous frequency c^{th} chirp-segment at time t_k . Since the instantaneous frequency of each chirp-segment is, by definition, a linear function of time, $f_{c,k}(\mathbf{x}_{c,k}) = f_{c,k}^{\text{int}} + \beta_{c,k}t_k$ we have that

$$\hat{f}_{c,k} = f_{c,k}^{\text{int}} + \beta_{c,k}t_k + \zeta_{f_{c,k}} \quad (22)$$

$$= \mathbf{H}_k \mathbf{x}_{c,k} + \zeta_{f_{c,k}} \quad (23)$$

where $\mathbf{H}_k = [1 \ t_k]$ is referred to as the model matrix. To account for the error induced on $\hat{f}_{c,k}$ by the random noise $\{w_{n,k}\}$ and the modeling error resulting from the STHM found in Equation (20), we include an Additive White Gaussian Noise (AWGN) error term $\zeta_{f_{c,k}}$ that we assume is zero mean with variance $\sigma_{\hat{f}_{c,k}}^2$. The

fact that $\zeta_{f_{c,k}}$ is assumed to be zero mean is equivalent to assuming that $\hat{f}_{c,k}$ is an unbiased estimator for $f_{c,k}$. This is a reasonable assumption since we ensure, by Step 6 in Section 2, that multiple frequency components within the same δ_k are well-separated and, therefore, avoid influence, or bias, due to spectral leakage from neighboring frequencies. Whiteness of $\zeta_{c,k}$ is justified if $\{w_n\}$ is white and the error terms are from different δ_k 's, but perhaps only approximately true otherwise. The assumption that $P_w(f)$ in each δ_k is slowly varying is, however a reasonable justification for why this assumption will hold approximately when $\{w_n\}$ is colored. Assuming that the noise has a Gaussian distribution is a convenient mechanism for developing the maximum likelihood solution. Finally, the estimation error variance $\sigma_{\hat{f}_{c,k}}^2$ can be approximated by [3, Eq. 477b, pg. 477]

$$\sigma_{\hat{f}_{c,k}}^2 \approx \frac{3}{N^3 \hat{R}_{c,k} (\pi T_s)^2} \quad (24)$$

where $\hat{R}_{c,k} = \frac{\hat{A}_{c,k}^2}{2\sigma_{w_{n,k}}^2}$ is an estimate of the SNR associated with the c^{th} sinusoid in the k^{th} time interval, and $\hat{\sigma}_{w_{n,k}}^2$ is the sample variance of the residuals $\hat{w}_{n,k} = r_{n,k} - \hat{s}_{n,k}$ where $\hat{s}_{n,k} = \sum_{c=1}^{\hat{L}_k} \hat{A}_{c,k} \cdot \cos(2\pi\hat{f}_{c,k}t_k + \hat{\phi}_{c,k})$. Then, $\left(\frac{\hat{f}_{c,k} - \mathbf{H}_k \mathbf{x}_{c,k}}{\sigma_{\hat{f}_{c,k}}}\right)^2$ is approximately Chi-Square distributed with one degree-of-freedom, and approximation we take to be an identity in what follows. With all the preliminaries in place we are now positioned to describe the 4 steps of the clustering algorithm. Before we do so we point out a simplification in notation that we will adopt throughout the remainder of this Section. In particular, we index the sample times and associated frequency estimates in \mathcal{S} with a single index, rather than the $(\cdot)_{c,k}$ used up to this point. As a result, when a time-interval δ_k gives rise to more than one frequency estimate there will be indices i and j , where $i \neq j$, such that $t_i = t_j$ and $\hat{f}_i \neq \hat{f}_j$. While this notation is generally more convenient, we will occasionally need to refer to the time interval δ_k that gave rise to a particular frequency estimate \hat{f}_i . To do so we define the mapping $\mathcal{I}(i) = k$, which is not one-to-one. This mapping amounts to book keeping in a computer implementation.

Step 1 – Compute Candidate Chirp-Segments: The first step is to compute all possible chirp-segment parameters from pairs of frequency estimates (\hat{f}_i, \hat{f}_j) , such that $|\mathcal{I}(i) - \mathcal{I}(j)| > g$, where $g > 0$ is a user-defined integer. This integer specifies the minimum number of time intervals that must separate frequency samples used to compute candidate chirp-segment parameters. A trade-off exists in the selection of g . Choosing g to be too small will result in an unnecessarily large computational burden since a very large number of candidates will result. Furthermore, solutions resulting from sample times too close together will be ill-conditioned. On the other hand, choosing g to be too large will limit the number of candidates available from which to form clusters. For the time-scales and sample-rates considered in this paper, $g = 5$ works well. Hence, the MLE of \mathbf{x}_{ij} [14, pg. 186] is

$$\hat{\mathbf{x}}_{ij} = \begin{bmatrix} \hat{f}_{ij}^{\text{int}} \\ \hat{\beta}_{ij} \end{bmatrix} = (\mathbf{H}_{ij}^T \mathbf{R}_{ij}^{-1} \mathbf{H}_{ij})^{-1} \mathbf{H}_{ij}^T \mathbf{R}_{ij}^{-1} \hat{\mathbf{f}}_{ij} \quad (25)$$

where $\mathbf{H}_{C_j} = [\mathbf{H}_{j_1} \cdots \mathbf{H}_{j_{|\mathcal{C}_j|}}]^T$, $\hat{\mathbf{f}}_{C_j} = [\hat{f}_{j_1} \cdots \hat{f}_{j_{|\mathcal{C}_j|}}]^T$, $\mathbf{R}_{C_j} = \begin{bmatrix} \sigma_{\hat{f}_{j_1}}^2 & \cdots & \mathbf{0} \\ \vdots & \ddots & \vdots \\ \mathbf{0} & \cdots & \sigma_{\hat{f}_{j_{|\mathcal{C}_j|}}}^2 \end{bmatrix}$ and the associated estimation error covariance is The associated estimation error covariance [14, pg. 186] is

$$\mathbf{P}_{ij} = E[(\mathbf{x} - \hat{\mathbf{x}}_{ij})(\mathbf{x} - \hat{\mathbf{x}}_{ij})^T] = (\mathbf{H}_{ij}^T \mathbf{R}_{ij}^{-1} \mathbf{H}_{ij})^{-1} \quad (26)$$

Each computed $\hat{\mathbf{x}}_{ij}$ and associated \mathbf{P}_{ij} are only considered chirp-segment candidates if the resulting $\hat{\beta}_{ij}$ is within a specified range of maximum and minimum allowable chirp-rates. In practice, chirp-rate can be bounded since the physical limitations of hardware will prohibit arbitrarily large or small chirp-rates.

Step 2 – Determine Frequency Estimates that are Statistically Similar to each Candidate: In this step we use the statistical distance metric known as the Mahalanobis distance to compare each frequency estimate from \mathcal{S} to each candidate chirp-segment computed in the previous step. Specifically, for frequency estimate \hat{f}_i , for $i = 1, \dots, N_{\text{est}}$, and chirp-segment candidate \mathbf{x}_j , where $j = 1, \dots, N_{\text{cand}}$, the Mahalanobis distance is $\mathcal{M}_{ij} = \left(\frac{\hat{f}_i - \mathbf{H}_j \hat{\mathbf{x}}_j}{\sigma_{\hat{f}_i}}\right)^2$, which has a χ_1^2 distribution when $\hat{\mathbf{x}}_j$ is the actual chirp-segment associated with \hat{f}_i . We use this fact to formulate a hypothesis test whose null hypothesis is that the frequency estimate \hat{f}_i falls on the candidate chirp-segment defined by $\hat{\mathbf{x}}_j$. Let α^C be the probability of Type I error (*i.e.*, the probability that the null hypothesis is rejected when it is true) and let γ be the critical value from the χ_1^2 distribution such that

$$\Pr(\chi_1^2 \leq \gamma) = \int_0^\gamma \chi_1^2(\xi) d\xi = 1 - \alpha^C \quad (27)$$

which can be determined numerically ** or using standard tables.¹⁵ So, we let \hat{f}_i be a member of cluster \mathcal{C}_j if $\mathcal{M}_{ij} \leq \gamma$, where \mathcal{C}_j is the set of indices such that $\mathcal{C}_j = \{i : \mathcal{M}_{ij} \leq \gamma\}$. Since the two indices associated with the frequency estimates used to compute $\hat{\mathbf{x}}_j$ from Equation (25) will always appear in \mathcal{C}_j , we require that the number of elements in a feasible cluster, denoted $|\mathcal{C}_j|$, be at least 3. Finally, we note that elements of \mathcal{C}_j are indexed by $j_1, \dots, j_{|\mathcal{C}_j|}$.

Step 3 – Find ML Cluster Among Feasible Clusters: The third step is to determine the ML cluster. This is accomplished by first using all frequency estimates in each cluster to compute a combined chirp-segment parameter estimate, $\hat{\mathbf{x}}_{\mathcal{C}_j}$. Based on this chirp-segment parameter estimate and the associated frequency estimates in \mathcal{C}_j we compute the likelihood value, \mathcal{L}_j .

First, we note that similar to Equation (25) the MLE of $\mathbf{x}_{\mathcal{C}_j}$ is

$$\hat{\mathbf{x}}_{\mathcal{C}_j} = \left(\mathbf{H}_{\mathcal{C}_j}^T \mathbf{R}_{\mathcal{C}_j}^{-1} \mathbf{H}_{\mathcal{C}_j} \right)^{-1} \mathbf{H}_{\mathcal{C}_j}^T \mathbf{R}_{\mathcal{C}_j}^{-1} \hat{\mathbf{f}}_{\mathcal{C}_j} \quad (28)$$

$$\text{where } \mathbf{H}_{\mathcal{C}_j} = \begin{bmatrix} \mathbf{H}_{j_1} & \cdots & \mathbf{H}_{j_{|\mathcal{C}_j|}} \end{bmatrix}^T, \hat{\mathbf{f}}_{\mathcal{C}_j} = \begin{bmatrix} \hat{f}_{j_1} & \cdots & \hat{f}_{j_{|\mathcal{C}_j|}} \end{bmatrix}^T, \mathbf{R}_{\mathcal{C}_j} = \begin{bmatrix} \sigma_{\hat{f}_{j_1}}^2 & \cdots & \mathbf{0} \\ \vdots & \ddots & \vdots \\ \mathbf{0} & \cdots & \sigma_{\hat{f}_{j_{|\mathcal{C}_j|}}}^2 \end{bmatrix} \text{ and}$$

the associated estimation error covariance is

$$\mathbf{P}_{\mathcal{C}_j} = \left(\mathbf{H}_{\mathcal{C}_j}^T \mathbf{R}_{\mathcal{C}_j}^{-1} \mathbf{H}_{\mathcal{C}_j} \right)^{-1} \quad (29)$$

Hence, the value of the likelihood function is

$$\mathcal{L}_j = \prod_{l=1}^{|\mathcal{C}_j|} \frac{1}{\sigma_{\hat{f}_{j_l}} \sqrt{2\pi}} e^{-\frac{1}{2} \left(\frac{\hat{f}_{j_l} - \mathbf{H}_{j_l} \hat{\mathbf{x}}_{\mathcal{C}_j}}{\sigma_{\hat{f}_{j_l}}} \right)^2} \quad (30)$$

which is equivalent to the PDF of $\hat{\mathbf{f}}_{\mathcal{C}_j}$ evaluated at $\hat{\mathbf{f}}_{\mathcal{C}_j}$ and $\hat{\mathbf{x}}_{\mathcal{C}_j}$. Hence, the cluster giving the largest likelihood value is

$$j_{\max} = \max_j \mathcal{L}_j \quad (31)$$

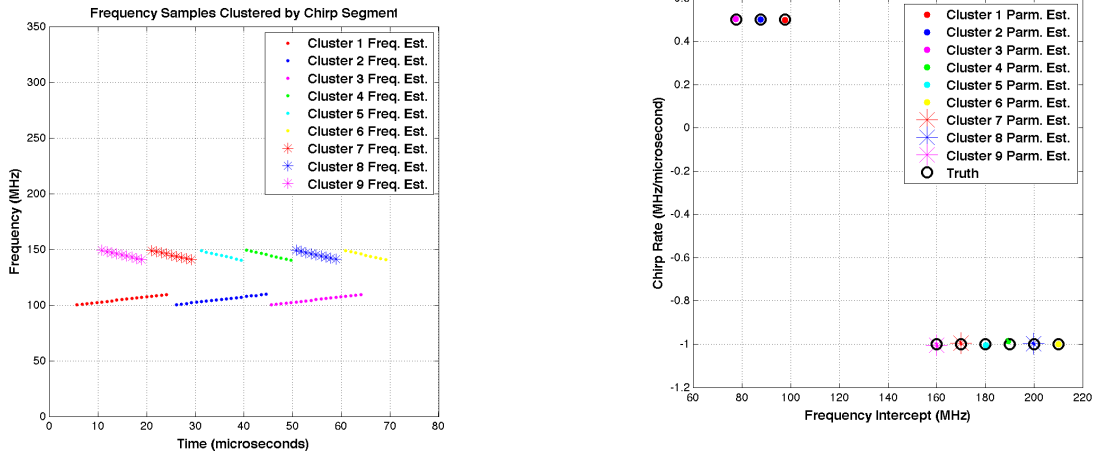
Step 4 – Retain ML Cluster Estimates and Remove Associated Frequency Estimates from \mathcal{S} : The fourth step is to retain the ML chirp segment estimate $\hat{\mathbf{x}}_{j_{\max}}$ and the associated estimation error covariance matrix $\mathbf{P}_{j_{\max}}$. Finally, we remove the elements of $\mathcal{C}_{j_{\max}}$ from \mathcal{S} and repeat Steps 1-3 until no candidate clusters are formed.

3.1.1 Clustering Example

In the remainder of this Section we apply the clustering approach just developed to the results from the example given in Section 2.2. In particular, we use the frequency estimates \hat{f}_i vs. sample time \hat{t}_i shown in Figure 3d as the elements of \mathcal{S} and attempt to find one cluster for each chirp-segment present in the data. In other words, if the clustering approach functions properly then we will produce nine clusters \mathcal{C}_j whose elements correspond to the indices associated with frequencies falling on the correct chirp-segment.

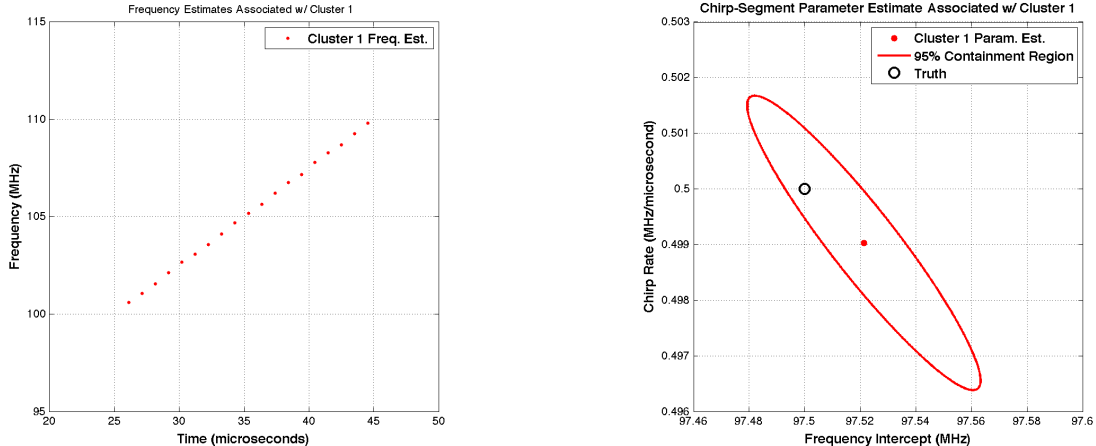
Figure 4 shows the clustering results in terms of the elements of each \mathcal{C}_j and the resulting $\hat{\mathbf{x}}_{\mathcal{C}_j}$, for $g = 5$ and $\alpha^C = 0.9999$. Figure 4a, which resembles 3d, shows the frequency estimates within each of the nine clusters automatically formed by the algorithm described in Steps 1-4 of this Section. Each color/marker-style combination corresponds to a unique \mathcal{C}_j . The most interesting result associated with Figure 4b is that all frequency estimates in \mathcal{S} were correctly associated with estimates of chirp-segment parameters that were very close to their true values. In other words, each \mathcal{C}_j contained frequency estimates from \mathcal{S} that resulted from the

**With the Statistics Toolbox in MATLAB®, the Chi-Squared critical value can be computed as $\gamma = \text{chi2inv}(1 - \alpha^C, \nu)$, where ν is the number of degrees of freedom and α is the probability of Type I error.



(a) Chirp-Segments Clustered by Frequency

(b) Chirp-Segment Parameter Estimates Associated with Each Frequency Cluster



(c) Zoomed-In View of Frequency Estimates Contained in Cluster 1

(d) Zoomed-In View of Chirp-Segment Parameter Estimates Resulting from Cluster 1

Figure 4: Clustering Example

associated true chip-segment, \mathbf{x}_j . Using the same color/marker-style combinations as Figure 4a, Figure 4b shows the chirp-segment parameter estimates computed via Equation (28) along with truth, \mathbf{x}_j . This figure is another way of showing that each of the 9 chirp-segments present in the data gave rise to a unique cluster that resulted in a chirp-segment parameter estimate that was very close to truth. Figure 4c is a zoomed-in view of the frequency estimates in \mathcal{C}_1 from Figure 4a and Figure 4d is a zoomed-in view of $\hat{\mathbf{x}}_{\mathcal{C}_1}$ from Figure 4b. In addition to truth and $\hat{\mathbf{x}}_{\mathcal{C}_1}$, Figure 4d shows the 95% containment region resulting from the estimation error covariance matrix given by Equation (29). The resulting ellipse is equivalent to the level-set of a bivariate Gaussian distribution with mean $\hat{\mathbf{x}}_{\mathcal{C}_1}$ and covariance $\mathbf{P}_{\mathcal{C}_1}$ that contains 95% of the total probability mass. The main takeaway from Figure 4d is that for this example and this cluster, all of the modeling assumptions leading up to it were accurate enough to produce estimates of $\hat{\mathbf{x}}_{\mathcal{C}_1}$ and $\mathbf{P}_{\mathcal{C}_1}$ that are statistically consistent since the ellipse contains truth. This same characteristic is true of the remaining 8 clusters. The observation of statistical consistency at this stage is compelling evidence for the validity of our modeling assumptions.

3.2 Association

The goal of the association stage is to associate \mathcal{C}_j 's corresponding to the same LFMCW signal. With reference to Figure 4a, if the association stage performs properly the five higher frequency chirp-segments will associate with one LFMCW signal and the remaining three lower frequency chirp-segments with associate with the other LFMCW signal. To accomplish this association within a statistical framework we will perform two hypothesis tests.

In the first hypothesis test we treat the samples within each \mathcal{C}_j as realizations from an unknown PDF. This view of the data motivates a hypothesis test where the null hypothesis is that frequency estimates contained in \mathcal{C}_i and \mathcal{C}_j are realizations from the same underlying PDF. Disproving this null hypothesis, and accepting the alternative hypothesis, amounts to concluding the data are from different PDF's. The most common approach for deciding between these hypotheses is the so-called Kolmogorov-Smirnov (KS) test [16, pgs. 620, 623-626]. The KS test statistic is

$$D_{ij}^{\text{KS}} = \max_{-\infty < f < \infty} |S_{\mathcal{C}_i}(f) - S_{\mathcal{C}_j}(f)| \quad (32)$$

where, for $|\mathcal{C}_j|$ frequency estimates $\hat{f}_{j_1}, \dots, \hat{f}_{j_{|\mathcal{C}_j|}}$, $S_{\mathcal{C}_j}(f)$ is the function that gives the fraction of estimates to the left of a given value f (*i.e.*, an estimate of the Cumulative Distribution Function (CDF)). Under the null hypothesis, the CDF of D_{ij}^{KS} can be closely approximated by a computable function. Thus, one can compute the probability that one would observe a value of the KS statistic D^{KS} that is less than the value computed from clusters \mathcal{C}_i and \mathcal{C}_j . That is, one rejects the null hypothesis if

$$\alpha^{\text{KS}} \leq \Pr(D^{\text{KS}} < D_{ij}^{\text{KS}}) \quad (33)$$

where α^{KS} is the significance level of the test ($\alpha^{\text{KS}} = 0.05$ is a common value) and

$$\Pr(D^{\text{KS}} < D_{ij}^{\text{KS}}) \approx Q_{\text{KS}} \left(\left[\sqrt{N_e} + 0.12 + 0.11/\sqrt{N_e} \right] \cdot D_{ij}^{\text{KS}} \right) \quad (34)$$

is a useful approximation to the CDF of D^{KS} ¹⁷ where

$$Q_{\text{KS}}(\lambda) = 2 \sum_{l=1}^{\infty} (-1)^{l-1} e^{-2l^2 \lambda^2} \quad (35)$$

$$N_e = \frac{|\mathcal{C}_i| \cdot |\mathcal{C}_j|}{|\mathcal{C}_i| + |\mathcal{C}_j|} \quad (36)$$

The second hypothesis test uses the estimation error variance associated with chirp-rate $\sigma_{\hat{\beta}_{\mathcal{C}_j}}^2$, contained in $\mathbf{P}_{\mathcal{C}_j}$, to formulate a chi-squared test that, under the null hypothesis, assumes $\hat{\beta}_{\mathcal{C}_i} = \hat{\beta}_{\mathcal{C}_j}$. The test statistic is

$$D_{ij}^{\beta} = \left(\frac{\hat{\beta}_{\mathcal{C}_i} - \hat{\beta}_{\mathcal{C}_j}}{\sigma_{\hat{\beta}_{\mathcal{C}_i}}} \right)^2 \quad (37)$$

which has a χ^2_1 distribution when $\hat{\beta}_{\mathcal{C}_j}$ is the true chirp-rate of the i^{th} chirp-segment. Hence, the critical value γ for a probability of Type I error α^β is computed as in Equation (27). The following steps implement the association approach.

Step 1 – Compute Test Statistics: For $i, j = 1, \dots, N_{\text{chirps}}$ compute D_{ij}^{KS} and D_{ij}^β .

Step 2 – Find ML Association Based on Chirp-Rate: For a fixed j and all i such that

$$\alpha^{\text{KS}} > Q_{\text{KS}} \left(\left[\sqrt{N_e} + 0.12 + 0.11/\sqrt{N_e} \right] \cdot D_{ij}^{\text{KS}} \right) \quad (38)$$

and $D_{ij}^\beta < \gamma$ (*i.e.*, \mathcal{H}_0 is accepted) compute the combined estimation error variance as $\sigma_{\hat{\beta}_j}^2 = \sum_i \frac{1}{\sigma_{\hat{\beta}_i}^2}$ and the combined chirp-rate estimate as $\hat{\beta}_j = \sigma_{\hat{\beta}_j}^2 \cdot \sum_i \frac{\hat{\beta}_i}{\sigma_{\hat{\beta}_i}^2}$. Based on these combined estimates, determine which set of associated chirp-segments maximizes its chirp-rate likelihood function

$$\mathcal{L}_j = \prod_{i=1} \frac{1}{\sqrt{2\pi} \cdot \sigma_{\hat{\beta}_j}} \cdot e^{-\frac{1}{2} \left(\frac{\hat{\beta}_i - \hat{\beta}_j}{\sigma_{\hat{\beta}_j}} \right)^2} \quad (39)$$

$$j_{\max} = \max_j \mathcal{L}_j \quad (40)$$

Let \mathcal{W}_m be the set containing $\hat{\beta}_{j_{\max}}$, $\sigma_{\hat{\beta}_{j_{\max}}}^2$, and all frequency estimates associated with \mathcal{C}_i . This set of parameter estimates and corresponding frequency estimates from each \mathcal{C}_i serves to represent the m^{th} LFMCW signal component.

Step 3 – Remove Contents of \mathcal{W}_m from Consideration and Recompute: Remove all $\hat{\beta}_i$, $\sigma_{\hat{\beta}_i}^2$, and associated \mathcal{C}_i corresponding to \mathcal{W}_m from consideration. If, after removal, only one \mathcal{C}_i remains, assign it and the associated $\hat{\beta}_{\mathcal{C}_i}$ and $\sigma_{\hat{\beta}_{\mathcal{C}_i}}^2$ to \mathcal{W}_M , then terminate. If, after removal, no \mathcal{C}_i remain, then terminate. Otherwise, repeat Steps 1-3.

3.2.1 Association Example

In the remainder of this section we apply the association approach developed above to the results obtained in Section 3.1.1. Figure 5 shows that the nine clusters formed from the steps outlined in Section 3.1 were correctly associated to two LFMCW signals. This is represented in the Figure by using red markers to denote all frequency samples associated to $s_1(t; \theta_1)$ and blue markers to denote all frequency samples associated to $s_2(t; \theta_2)$.

3.3 Estimation

At this stage in the algorithm it is worthwhile to remind ourselves what our goal is and what we have at our disposal. The goal is to estimate the parameters of Equation (15) given in Equation (17). So far we have at our disposal estimates of the instantaneous frequency of each $s_m(t; \theta_m)$, estimates of their associated chirp-rates, and the estimation error variance of these chirp-rates. In this section we propose a method, which we refer to as *initial* estimation, for estimating the elements of $\bar{\theta}_m$. We then use these initial estimates as the initial conditions to a numerical implementation of MLE originally derived in¹ to refine each of these parameters. This approach, in contrast to,² is computationally tractable for $M > 1$. We also note that while these estimates are referred to as “initial”, they may be sufficiently accurate for some applications. If very high accuracy is not required, then computational requirements can be drastically reduced by avoiding the MLE search all together.

To obtain the initial estimates of $\bar{\theta}_m$, denoted $\hat{\theta}_m^0$, let the true instantaneous frequency of $s_m(t; \bar{\theta}_m)$ at the sample times in \mathcal{W}_m , denoted $t_{m,i}$, be given by $f_{m,i} = f_m^{\text{start}} + \beta_m \text{ mod } (t_{m,i} + \Delta_m, T_{p,m})$ and let the associated

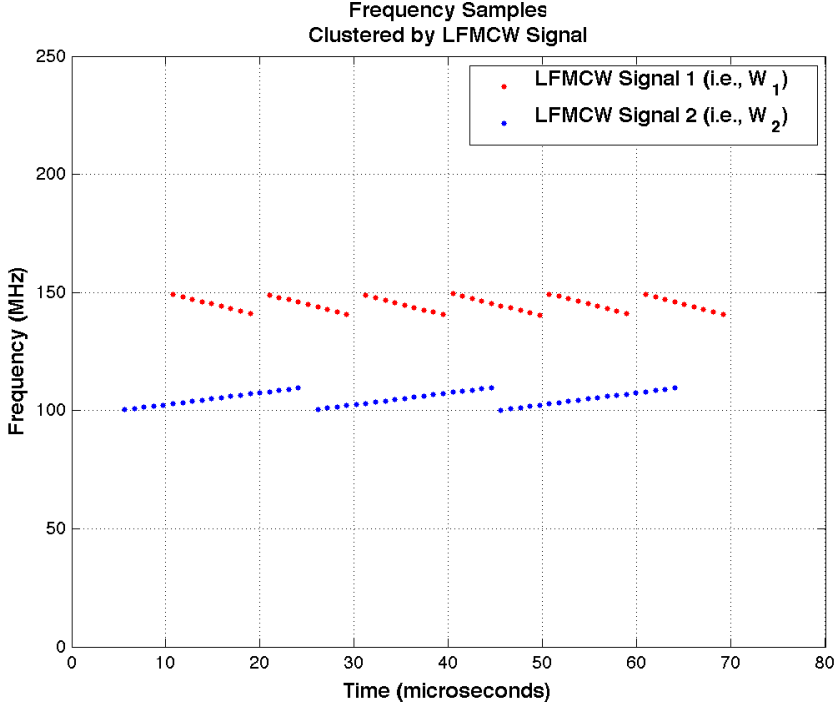


Figure 5: Association Example

frequency estimates in \mathcal{W}_m be denoted by $\hat{f}_{m,i}$, for $i = 1, \dots, N_m$, where N_m is the number of frequency estimates in \mathcal{W}_m . Then we can obtain initial estimates of f_m^{start} , β_m , Δ_m , and $T_{p,m}$ by solving the following optimization problem

$$\min_{f_m^{\text{start}}, \beta_m, \Delta_m, T_{p,m}} \left\{ \sum_{i=1}^{N_m} |\hat{f}_{m,i} - f_{m,i}| \right\} \quad (41)$$

Unfortunately, since the objective function in Equation (41) is not only non-differentiable but also nonlinear, standard optimization techniques based on gradients of the objective function will likely fail. Therefore, to obtain initial estimates of f_m^{start} , β_m , Δ_m , and $T_{p,m}$ we implement the Nelder-Mead simplex direct search algorithm,¹⁸ which is a so-called “derivative-free” method. Finally, we can obtain initial estimates of τ_m and t_m^{stop} by taking them to be $\hat{\tau}_m^0 = \min_i t_{m,i}$ and $\hat{t}_m^{\text{stop},0} = \max_i t_{m,i}$.

To obtain refined estimates of $\bar{\theta}_m$, denoted $\hat{\theta}_m$, we implement the MLE found in Equation (3), which came from.¹ As in¹ and,² if one begins with Equation (3) and attempts a brute force search over all $\bar{\theta}$, the computational burden that results makes practical implementation impossible when $M > 1$; an observation clearly stated throughout.² To circumvent this limitation we implement the MLE with $\hat{\theta}^0 = [\hat{\theta}_1^{0T} \dots \hat{\theta}_M^{0T}]^T$ as initial conditions and the associated estimation error variances, when available, to limit the search space. In addition, we note that if we hold all other parameters fixed, Equation (3) can be computed for all τ_m to a resolution on the order of T_s using the FFT algorithm since Equation (3) reduces to a 1-D temporal correlation in this case, which has a well-known implementation based on the FFT.¹⁹

3.3.1 “Initial” Estimation Example

In this example initial estimates of $\bar{\theta}_1$ and $\bar{\theta}_2$ are obtained by computing $\hat{\tau}_m^0$, $\hat{t}_m^{\text{stop},0}$, and solving the optimization problem posed in Equation (41) by using MATLAB’s® implementation of the Nelder-Mead simplex direct search algorithm found in the Optimization Toolbox. The results are summarized in Table 3.

Table 3: Initial Estimation Results

Parameter	θ_1	$\hat{\theta}_1^0$	θ_2	$\hat{\theta}_2^0$	Units
τ_m^0	5	5.6320	10	10.752	μs
$t_m^{0,\text{stop}}$	65	64.000	70	69.120	μs
$f_m^{0,\text{start}}$	100	99.804	150	150.172	MHz
β_m^0	0.5	0.49850	-1.0	-0.99840	MHz
Δ_m^0	15	15.466	10	10.163	μs
$T_{p,m}^0$	20	20.020	10	9.9964	μs

3.3.2 Fine Estimation Example

In this example we use the results from Section 3.3.1 as initial conditions to a grid search over Equation (3). For simplicity we limit our search space to $\hat{\tau}_m$ and \hat{f}_m^{start} , where the search over $\hat{\tau}_m$ is

$$\hat{\tau}_m^c - \hat{T}_{p,m}^c / 4 \leq \hat{\tau}_m \leq \hat{\tau}_m^c + \hat{T}_{p,m}^c / 4 \quad (42)$$

and over \hat{f}_m^{start} is

$$\hat{f}_m^{\text{c,start}} - 15\sigma_{\hat{f}_m}^{\max} / 2 \leq \hat{f}_m^{\text{start}} \leq \hat{f}_m^{\text{c,start}} + 15\sigma_{\hat{f}_m}^{\max} / 2 \quad (43)$$

where $\sigma_{\hat{f}_m}^{\max}$ is the maximum frequency standard deviation computed according to Equation (24) for the m^{th} LFM CW signal. The TOA dimension was computed using an $N_{\text{FFT}} = 2^{16}$ point FFT for each of 2001 equally spaced points in the range defined by Equation (43). To further simplify the computation we decoupled the search so that $\hat{\theta}_1$ was computed using a discretized version of

$$\hat{\theta}_1 = \max_{\tau_1, f_1^{\text{start}}} \left| \int_0^T r(t) s_1^*(t; \bar{\theta}_1) dt \right|^2 \quad (44)$$

and $\hat{\theta}_2$ was computed using a discretized version of

$$\hat{\theta}_2 = \max_{\tau_2, f_2^{\text{start}}} \left| \int_0^T r(t) s_2^*(t; \bar{\theta}_2) dt \right|^2 \quad (45)$$

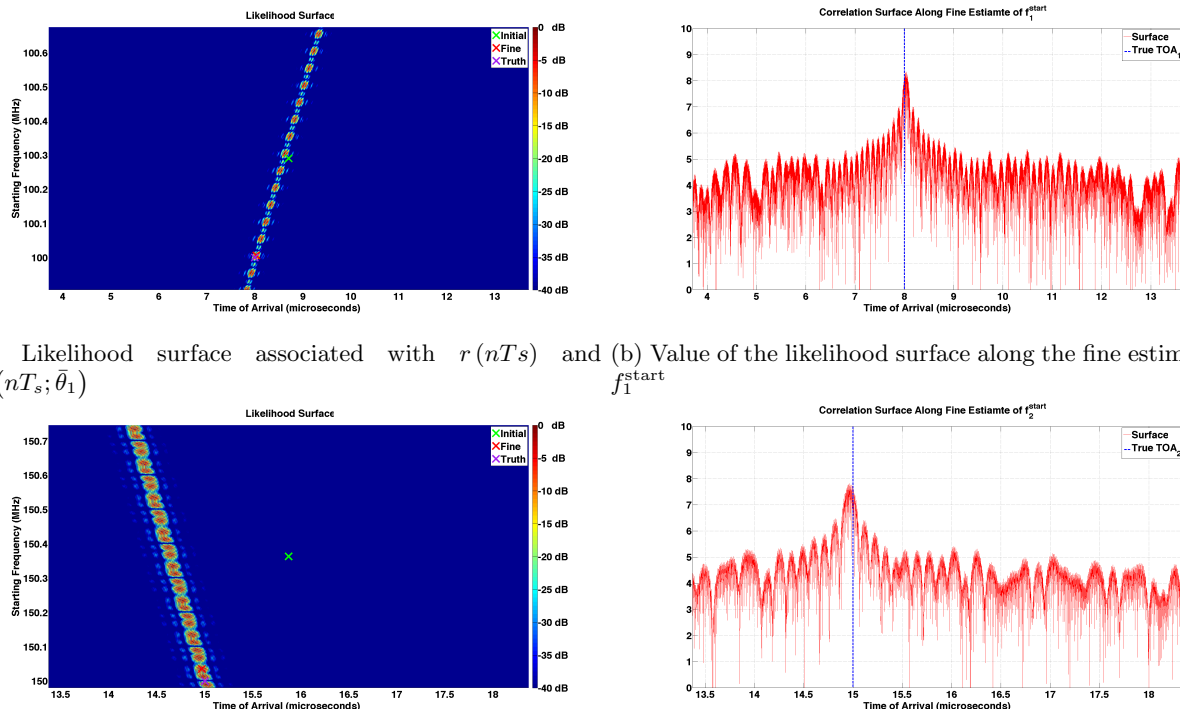
The fine estimation results are summarized in Table 4 and the arguments of the right hand sides of Equations (44) and (45) are plotted in Figures 6a and 6c, respectively. The intensity of each point in Figures 6a and 6c is proportional to the value of the likelihood function evaluated at the corresponding parameter values. These images show how evaluating the likelihood function in search of an approximate MLE can improve the initial estimates since the fine estimates are closer to truth. We also note that the shape of the likelihood surface is not only non-convex, but also multi-modal. Both of these characteristics will complicate gradient-search based efforts to improve computational speed. Figures 6b and 6d show the value of the likelihood function along the fine estimates of f_1^{start} and f_2^{start} , respectively.

4. LOCALIZATION

While the use of Time Difference of Arrival (TDOA) in a passive sensor network is not a new *concept* for locating Electromagnetic (EM) signal sources, successful *implementation* is often complicated by any number of hardware or environmental limitations. One common approach for obtaining TDOA estimates is to cross correlate two sampled versions of the same transmitted signal, taken at spatially separated receivers, and use the peak of the cross correlation as the estimator for TDOA. This approach, which is explained in detail in²⁰ and,²¹ is attractive

Table 4: Fine Estimation Results

Parameter	θ_1	$\hat{\theta}_1$	θ_2	$\hat{\theta}_2$	Units
τ_m	5	4.9340	10	9.9800	μs
f_m^{start}	100	99.996	150	150.019	MHz



(a) Likelihood surface associated with $r(nTs)$ and (b) Value of the likelihood surface along the fine estimate of $s_1(nTs; \bar{\theta}_1)$

(c) Likelihood Surface Associated with $r(nTs)$ and (d) Value of the likelihood surface along the fine estimate of $s_2(nTs; \bar{\theta}_2)$

Figure 6: Estimation Example

when hardware to support high bandwidth data links is available for the transmission of the data samples taken at each node to a central node that performs the cross correlation. This type of TDOA estimation is especially useful when very little is known, or needs to be known, about the detailed structure of the signal. However, this approach becomes less attractive when the number of signals residing in the operating bandwidth of the receiver is large or when the interference (*i.e.*, extraneous signals that are not of interest) environment becomes dense. Furthermore, if one has general knowledge of the structure of the signal, like that which we assume of the LFM CW signal modeled in Equation (15), cross correlation provides no means for exploiting this information to improve processing accuracy or to aid ambiguity resolution that inevitably arises in a multi-source environment.

If the structure of the transmitted signal is known, but the time the signal began to transmit is unknown an alternative method for obtaining TDOA is available that is better suited to multi-source environments. In particular, one can design a matched filter, which is the MLE of TOA, to estimate the TOA of each source at each receiver in the network. Then, upon transmission of only the parameters that define the signal structure to a central node, in particular TOA, TOA differences can be taken to eliminate the unknown transmit time and yield TDOA estimates, which are a function of only the source's position and the positions of receivers. Furthermore, since matched filtering is equivalent to correlating a known signal with an observed signal, additive interference components present in the observed signal that are uncorrelated with the signal defining the matched filter tend to have little effect on the output. In other words, interference that is uncorrelated with the EM source of interest is naturally suppressed. It is this approach to generating estimates of TDOA that we pursue since our implementation of Equation (3) in Section 3.3 can be viewed as an approximate matched filter. An additional benefit of our approach to TDOA generation and source localization is that since each TOA estimate is an element of the parameter vector $\hat{\theta}_m$, association of TOA estimates to the same source can be aided by the other parameters that define the signal structure of the source. Associating observations to the same source is referred to as the *data association* problem, and is a major undertaking in all multi-source localization applications.²² Our approach naturally provides additional information, often referred to as features in the multi-target tracking literature, that can improve data association performance.

4.1 Measurement Model

In this section we develop the measurement model that relates estimates of TOA $\hat{\tau}_m$ obtained in Section 3.3 to TDOA, and ultimately to the latitude and longitude of the each LFM CW source. In order to do this we need at least three stationary or two moving receivers collaborating in the sensor network with synchronized clocks and an ability to resolve their own Earth Centered Earth Fixed (ECEF)²³ position. We denote an estimate of the TOA of the m^{th} LFM CW source taken by the i^{th} receiver as $\hat{\tau}_{m,i}$, where $i = 1, \dots, N_{rx}$ and N_{rx} is the number of receivers.

Let $t = 0$ be defined as the common time at which all receivers begin to sample the signal environment and $t_{m,0}$ be defined as the time, relative to $t = 0$, at which the m^{th} source begins to transmit. Hence, the true TOA of the m^{th} LFM CW source, observed by the i^{th} receiver is

$$\tau_{m,i} = t_{m,0} + r_{m,i}/c \quad (46)$$

where $r_{m,i} = \|\mathbf{p}_{s,m} - \mathbf{p}_{rx,i}\|$ is the range from the m^{th} LFM CW source to the i^{th} receiver, $\|\cdot\|$ denotes the Euclidean vector norm, $\mathbf{p}_{s,m}$ is the ECEF position vector of the m^{th} source, $\mathbf{p}_{rx,i}$ is the ECEF position vector of the i^{th} receiver, and c is the speed of light. TDOA can then be expressed as

$$TDOA_m^{ij} = \tau_{m,i} - \tau_{m,j} \quad (47)$$

$$= t_{m,0} + r_{m,i}/c - t_{m,0} - r_{m,j}/c \quad (48)$$

$$= (r_{m,i} - r_{m,j})/c \quad (49)$$

where $i, j = 1, \dots, N_{rx}$. We can relate the unknown position of the m^{th} source to $TDOA_m^{ij}$ using our knowledge of the ECEF²³ position of the i^{th} receiver $\mathbf{p}_{rx,i}$. Hence, Equation (49) can be rewritten as

$$TDOA_m^{ij} = (r_{m,i} - r_{m,j})/c \quad (50)$$

$$= \|\mathbf{p}_{s,m} - \mathbf{p}_{rx,i}\| - \|\mathbf{p}_{s,m} - \mathbf{p}_{rx,j}\| \quad (51)$$

As the name implies, the ECEF position of an object is defined relative to the earth's center and, therefore, is not constrained to the earth's surface. Since we are interested in estimating the location of stationary, ground-based LPI radar systems we can incorporate the shape of the earth as a constraint on the position by employing a model of the earth's surface. A particularly popular choice is the World Geodetic System 1984 (WGS84) earth model,²³ which models the earth's surface as an oblate spheroid (ellipsoid) and allows position on the earth's surface to be represented using the angles longitude and geodetic latitude. In particular, the WGS84 earth model relates ECEF position to latitude Ψ and longitude Φ as

$$\mathbf{p}(\mathbf{q}) = \begin{bmatrix} (r_E + a) \cos(\Psi) \cos(\Theta) \\ (r_E + a) \sin(\Psi) \cos(\Theta) \\ (r_E (1 - ecc^2) + a) \sin(\Theta) \end{bmatrix} \quad (52)$$

where $q = [\Psi \ \Theta]^T$, a is the altitude above the WGS84 ellipsoid, and ecc is the earth's eccentricity. The term r_E is the earth's transverse radius of curvature defined by

$$r_E = \frac{r_{eq}}{\sqrt{1 - ecc^2 \sin^2(\Theta)}} \quad (53)$$

where r_{eq} is the earth's radius at the equator. Finally, we can rewrite Equation (51) as

$$\text{TDOA}_m^{ij} = \|\mathbf{p}_{s,m} - \mathbf{p}_{rx,i}\| - \|\mathbf{p}_{s,m} - \mathbf{p}_{rx,j}\| \quad (54)$$

$$= \|\mathbf{p}(\mathbf{q}_{s,m}) - \mathbf{p}_{rx,i}\| - \|\mathbf{p}(\mathbf{q}_{s,m}) - \mathbf{p}_{rx,j}\| \quad (55)$$

$$= h(\mathbf{q}_{s,m}; \mathbf{p}_{rx,i}, \mathbf{p}_{rx,j}) \quad (56)$$

In our localization approach we will assume that the altitude of each LFMCW source is either known or can be closely approximated by a constant value. This is typically a reasonable assumption in passive ELINT applications and will lead to algorithms for estimating $\mathbf{q}_{s,m}$ that are extremely stable and rapidly convergent.²⁴ However, if the terrain particularly mountainous, making the assumption of locally constant altitude invalid, one can incorporate terrain information, such as that found in Digital Terrain and Elevation Data (DTED), a data product published by the Department of Defense (DoD).

Equation (56) leads to the following model of the TDOA measurements associated with the m^{th} LFMCW source

$$\mathbf{z}_m = \mathbf{h}(\mathbf{q}_{s,m}; \mathbf{p}_{rx}) + \mathbf{v}_m \quad (57)$$

where $\mathbf{h}(\mathbf{q}_{s,m}; \mathbf{p}_{rx})$ is an $N_{meas} \times 1$ vector-valued function with elements defined by Equation (56) and length determined by the number of unique pairwise sensor node combinations. The term \mathbf{v}_m is also $N_{meas} \times 1$ and models the errors associated with the TDOA estimates, which we take to be independent Gaussian random variables with covariance \mathbf{R}_m .

4.2 Iterated Least-Squares

One approach to computing $\mathbf{q}_{s,m}$ is by solving the following optimization problem

$$\min_{\mathbf{q}_{s,m}} (\mathbf{z}_m - \mathbf{h}(\mathbf{q}_{s,m}; \mathbf{p}_{rx}))^T \mathbf{R}_m^{-1} (\mathbf{z}_m - \mathbf{h}(\mathbf{q}_{s,m}; \mathbf{p}_{rx})) \quad (58)$$

which amounts to solving a set of nonlinear equations for $\mathbf{q}_{s,m}$. Since the argument in Equation (58) is a differentiable function of $\mathbf{q}_{s,m}$, numerous numerical methods exist for determining the $\mathbf{q}_{s,m}$ that minimizes Equation (58).²⁵ The most popular of these is Newton's method, and a simplification of Newton's method known as Iterated Least-Squares (ILS), which we overview in what follows.

To implement ILS two main pieces of information are required. First, since ILS is an iterative approach, initial conditions for $\mathbf{q}_{s,m}$ are needed, which can be obtained via a coarse grid search of Equation (58). Second, the gradient of $\mathbf{h}(\mathbf{q}_{s,m}; \mathbf{p}_{rx})$ with respect to $\mathbf{q}_{s,m}$ is required, which is

$$\frac{\partial \mathbf{h}(\mathbf{q}_{s,m}; \mathbf{p}_{rx})}{\partial \mathbf{q}_{s,m}} = \frac{\partial \mathbf{h}(\mathbf{q}_{s,m}; \mathbf{p}_{rx})}{\partial \mathbf{p}(\mathbf{q}_{s,m})} \frac{\partial \mathbf{p}(\mathbf{q}_{s,m})}{\partial \mathbf{q}_{s,m}} \quad (59)$$

where the l^{th} row of $\frac{\partial \mathbf{h}(\mathbf{q}_{s,m}; \mathbf{p}_{rx})}{\partial \mathbf{p}(\mathbf{q}_{s,m})}$ is given by

$$\frac{\partial h_l(\mathbf{q}_{s,m}; \mathbf{p}_{rx})}{\partial \mathbf{p}(\mathbf{q}_{s,m})} = \frac{h(\mathbf{q}_{s,m}; \mathbf{p}_{rx,i}, \mathbf{p}_{rx,j})}{\partial \mathbf{p}(\mathbf{q}_{s,m})} \quad (60)$$

$$= \mathbf{u}_i^T - \mathbf{u}_j^T \quad (61)$$

$$(62)$$

The term \mathbf{u}_i is a unit vector pointing from receiver i to the source location, with \mathbf{u}_i being similarly defined for receiver j . Specifically,

$$\mathbf{u}_i = \frac{\mathbf{p}(\mathbf{q}_{s,m}) - \mathbf{p}_{rx,i}}{\|\mathbf{p}(\mathbf{q}_{s,m}) - \mathbf{p}_{rx,i}\|} \quad (63)$$

$$\mathbf{u}_j = \frac{\mathbf{p}(\mathbf{q}_{s,m}) - \mathbf{p}_{rx,j}}{\|\mathbf{p}(\mathbf{q}_{s,m}) - \mathbf{p}_{rx,j}\|} \quad (64)$$

Next, the partial derivative of the source's ECEF position with respect to its longitude and latitude is

$$\frac{\partial \mathbf{p}(\mathbf{q}_{s,m})}{\partial \mathbf{q}_{s,m}} = \left[\begin{array}{c} \frac{\partial \mathbf{p}(\mathbf{q}_{s,m})}{\partial \Psi} \quad \frac{\partial \mathbf{p}(\mathbf{q}_{s,m})}{\partial \Theta} \end{array} \right] \quad (65)$$

where

$$\frac{\partial \mathbf{p}(\mathbf{q}_{s,m})}{\partial \Psi} = \left[\begin{array}{c} \frac{\partial a}{\partial \Psi} \cos(\Psi) \cos(\Theta) - (r_E + a) \sin(\Psi) \cos(\Theta) \\ \frac{\partial a}{\partial \Psi} \sin(\Psi) \cos(\Theta) + (r_E + a) \cos(\Psi) \cos(\Theta) \\ \frac{\partial a}{\partial \Psi} \sin(\Theta) \end{array} \right] \quad (66)$$

$$\frac{\partial \mathbf{p}(\mathbf{q}_{s,m})}{\partial \Theta} = \left[\begin{array}{c} \left(\frac{\partial r_E}{\partial \Theta} + \frac{\partial a}{\partial \Theta} \right) \cos(\Psi) \cos(\Theta) - (r_E + a) \cos(\Psi) \sin(\Theta) \\ \left(\frac{\partial r_E}{\partial \Theta} + \frac{\partial a}{\partial \Theta} \right) \sin(\Psi) \cos(\Theta) - (r_E + a) \sin(\Psi) \sin(\Theta) \\ \left(\frac{\partial r_E}{\partial \Theta} (1 - ecc^2) + \frac{\partial a}{\partial \Theta} \right) \sin(\Theta) + (r_E (1 - ecc^2) + a) \cos(\Theta) \end{array} \right] \quad (67)$$

$$\frac{\partial r_E}{\partial \Theta} = \frac{ecc^2 \sin(\Theta) \cos(\Theta) r_E}{1 - ecc^2 \cdot \sin^2(\Theta)} \quad (68)$$

and

$$\frac{\partial a}{\partial \Psi} = \frac{\partial a}{\partial \Theta} = 0 \quad (69)$$

if altitude is constant.

Let $\hat{\mathbf{q}}_{s,m}^0$ denote the initial conditions for the m^{th} source location and

$$\mathbf{H}_m = \left. \frac{\partial \mathbf{h}(\mathbf{q}_{s,m}; \mathbf{p}_{rx})}{\partial \mathbf{q}_{s,m}} \right|_{\hat{\mathbf{q}}_{s,m}, \mathbf{p}_{rx}} \quad (70)$$

be the gradient of \mathbf{h} evaluated at the current estimate of the m^{th} source location $\hat{\mathbf{q}}_{s,m}$ and the locations of the receivers, \mathbf{p}_{rx} . Then localization via ILS can be summarized by the following steps:

Step 0 – Initialization: Select a range of latitude and longitude values that will contain the m^{th} source location and discretize the region. Evaluate the argument of Equation (58) for each grid point and select $\hat{\mathbf{q}}_{s,m}^0$ to be the grid point yielding the smallest value of the argument of Equation (58) and let $\hat{\mathbf{q}}_{s,m}^0 = \hat{\mathbf{q}}_{s,m}^{old}$. This step need only be performed once.

Step 1 – Update Gradient: Compute \mathbf{H}_m with $\hat{\mathbf{q}}_{s,m}^{old}$.

Step 2 – Update Source Location Estimate:

$$\hat{\mathbf{q}}_{s,m}^{new} = \hat{\mathbf{q}}_{s,m}^{old} + [\mathbf{H}_m^T \mathbf{R}_m^{-1} \mathbf{H}_m]^{-1} \mathbf{H}_m^T \mathbf{R}_m^{-1} (\mathbf{z}_m - \mathbf{h}(\hat{\mathbf{q}}_{s,m}^{old}; \mathbf{p}_{rx})) \quad (71)$$

Step 3 – Check for Convergence: If $\|\mathbf{p}(\hat{\mathbf{q}}_{s,m}^{old}) - \mathbf{p}(\hat{\mathbf{q}}_{s,m}^{new})\| < tol$ then terminate. Otherwise, let $\hat{\mathbf{q}}_{s,m}^{old} = \hat{\mathbf{q}}_{s,m}^{new}$ and repeat Steps 1-3.

Once the iteration terminates one can approximate the estimation error covariance matrix of $\hat{\mathbf{q}}_{s,m}^{new}$ by performing a Taylor Series expansion on $\mathbf{h}(\mathbf{q}_{s,m}; \mathbf{p}_{rx})$ about $\hat{\mathbf{q}}_{s,m}^{old}$

$$\mathbf{h}(\mathbf{q}_{s,m}; \mathbf{p}_{rx}) \approx \mathbf{h}(\hat{\mathbf{q}}_{s,m}^{old}; \mathbf{p}_{rx}) + \mathbf{H}_m (\mathbf{q}_{s,m} - \hat{\mathbf{q}}_{s,m}^{old}) \quad (72)$$

From this point forward we take the approximation given in Equation (72) to be an equality. Then substitution into Equation (57) yields

$$\mathbf{z}_m - \mathbf{h}(\hat{\mathbf{q}}_{s,m}^{old}; \mathbf{p}_{rx}) = \mathbf{H}_m (\mathbf{q}_{s,m} - \hat{\mathbf{q}}_{s,m}^{old}) + \mathbf{v}_m \quad (73)$$

Next, substituting Equation (73) into Equation (71) yields

$$\hat{\mathbf{q}}_{s,m}^{new} = \mathbf{q}_{s,m} + \mathbf{K}_m \mathbf{v}_m \quad (74)$$

where

$$\mathbf{K}_m = [\mathbf{H}_m^T \mathbf{R}_m^{-1} \mathbf{H}_m]^{-1} \mathbf{H}_m \mathbf{R}_m^{-1} \quad (75)$$

Then

$$\mathbf{P}_{s,m} = E \left[(\mathbf{q}_{s,m} - \hat{\mathbf{q}}_{s,m}^{new}) (\mathbf{q}_{s,m} - \hat{\mathbf{q}}_{s,m}^{new})^T \right] \quad (76)$$

$$= \mathbf{K}_m \mathbf{R}_m \mathbf{K}_m^T \quad (77)$$

After some simplification $\mathbf{P}_{s,m}$ can be expressed as

$$\mathbf{P}_{s,m} = [\mathbf{H}_m^T \mathbf{R}_m^{-1} \mathbf{H}_m]^{-1} \quad (78)$$

4.3 Localization Example

In this section we use the localization approach just described to locate two LPI radars in a maritime environment using three stationary receivers. The true locations of the radars and receivers for this test scenario ^{††} are shown in Figure 7. We assume the parameters that define signals $m = 1, 2$, which are given in Table 3, correspond to the transmissions from radars 1 and 2, respectively. In addition to employing the localization method just described to estimate the latitude and longitude of each radar, we assume that receivers 1, 2, and 3 use the detection processing described in Section 2 and the characterization processing described in Section 3 to obtain estimates of $\bar{\theta}_{m,i}$, where $i = 1, 2, 3$ the receiver indices. The estimates of TOA that result are used to form TDOA estimates as shown in Equation (47).

The SNR of each LFMCW signal component at each receiver was computed using a link-budget similar to that detailed in [10, Ch. 4]. In particular

$$\text{SNR}_{m,i} = \frac{P_{m,i}}{\mathcal{N}_i} \quad (79)$$

where $P_{m,i}$ is the received power of the m^{th} source at the i^{th} receiver and \mathcal{N}_i is the noise power imposed by the i^{th} receiver. The received power is

$$P_{m,i} = \frac{\text{EIRP}_m \lambda_m^2 G_{m,i}}{(4\pi d_{m,i})^2} \quad (80)$$

where EIRP _{m} is the Effective Isotropically Radiated Power of the m^{th} source, λ_m is the wavelength of the carrier frequency of the m^{th} source, $G_{m,i}$ is the gain of the i^{th} receiver's antenna in the direction of the m^{th} source, and $d_{m,i}$ is the distance between the m^{th} source and the i^{th} receiver. We take the EIRP of each radar to be 1 Watt, their carrier frequencies to be 10 GHz, and each receiver gain $G_{m,i}$ to be 10 dB. The distance between each radar and each receiver $d_{m,i}$ is computed using the associated true values, which are summarized in Tables

^{††}The region near Palermo, Italy was chosen only because the geography of its port was convenient.

Table 5: True Radar Locations

	Radar 1	Radar 2	Units
Longitude Ψ	13.400177	13.373398	Degrees
Latitude Θ	38.100253	38.151837	Degrees
Altitude a	100	100	Feet

Table 6: Receiver Locations

	Receiver 1	Receiver 2	Receiver 3	Units
Longitude Ψ	13.590034	13.515877	13.418030	Degrees
Latitude Θ	38.134287	38.189895	38.251662	Degrees
Altitude a	3	3	3	Feet

5 and 6. To relate the received power predicted by the link-budget to s_m as defined in Equation (15) we note that since the signal is periodic with period $T_{p,m}$ it is a power signal with power given by

$$P_{m,i} = \frac{1}{T_{p,m}} \int_{T_{p,m}} \left(b_{m,i} \cos \left(2\pi f_m t + \pi \beta_m \bmod(t + \Delta_m, T_{p,m})^2 \right) \right)^2 dt \quad (81)$$

$$= \frac{b_{m,i}^2}{2} \quad (82)$$

where the integral is taken over one full period of the m^{th} LFMCW signal. Hence,

$$b_{m,i} = \sqrt{\frac{\text{EIRP}_m \lambda_m^2 G_{m,i}}{2 (4\pi d_{m,i})^2}} \quad (83)$$

The noise power contributed by the i^{th} receiver is

$$\mathcal{N}_i = kTB_i \cdot \text{NF}_i \quad (84)$$

where k is Boltzmann's constant, $T = 290$ K is the standard noise temperature, B_i is the noise-equivalent bandwidth of the i^{th} receiver, and NF_i is the Noise Figure of the i^{th} receiver. For each receiver we take B_i to be 50 MHz and N_i to be 6dB. The noise power predicted by the receiver model can then be related to the noise model $w(t)$ defined in Equation (13) simply by letting

$$\mathcal{N}_i = \sigma_{w,i}^2 \quad (85)$$

For simplicity we assume the noise is uncorrelated from sample to sample and Gaussian distributed with zero mean. While this is simpler for simulation it is not a necessary condition given our development in Section 2. Hence,

$$\sigma_{w,i} = \sqrt{kTB_i \cdot \text{NF}_i} \quad (86)$$

The results are summarized in Table 7 and Figure 8. Table 7 gives the miss distance between the true radar location and the estimated radar location for each radar. Additionally, we give the semi-major and semi-minor

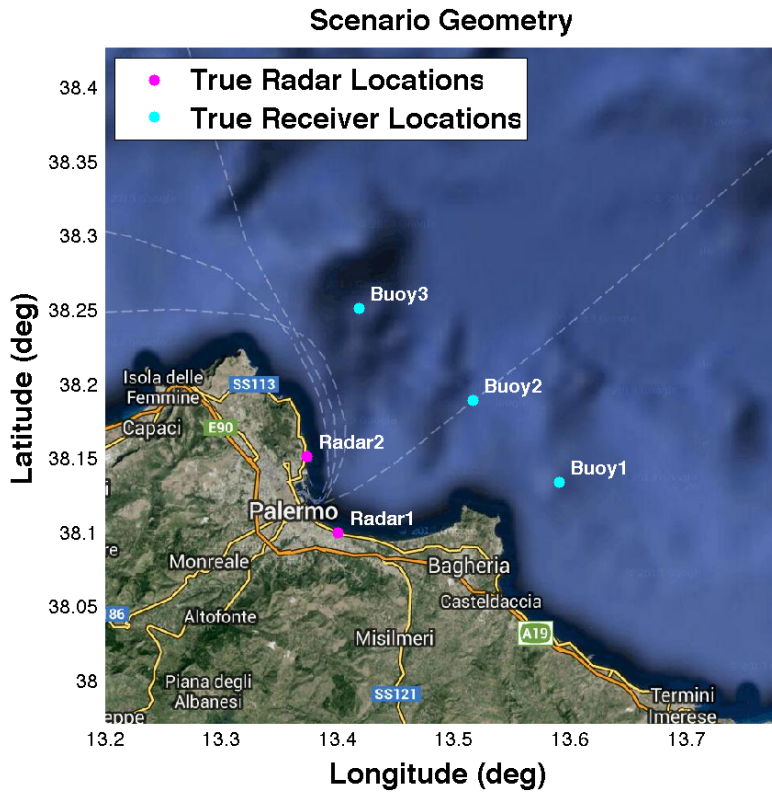


Figure 7: Localization Scenario

axis lengths associated with the ellipses shown in Figures 8b and 8d. These ellipses are computed by assuming that the solution converged to by ILS is the mean of a Gaussian random variable with covariance given by Equation (78). The ellipse is then equivalent to a level set of a bivariate Gaussian PDF and its size is determined by the probability that the true target is contained within the ellipse, which we take to be 95% for this example. For a fixed probability of containment, the size and orientation of the ellipse is driven largely by the number and orientation of the receivers relative to each radar.

In addition to the radar locations and their respective uncertainties as represented by the 95 % containment regions, Figures 8a-8d show the value of the argument of Equation (58) computed for each value of latitude and longitude within the plotted regions. As expected, the estimate of the target location is in a region where the objective function is small. Additionally, we plot the TDOA isograms²⁶ corresponding to each TDOA estimate computed using the methods from Sections 2 and 3. A TDOA isogram is the set of all latitude and longitude values that satisfy Equation (56). As expected, the intersection of two TDOA isograms computed based on estimated TOA's corresponds to the latitude and longitude of the estimated target location. Finally, we note that if only three receivers are available then two TDOA estimates result, which, for this configuration, gives rise to a second intersection on the side of the receivers further from the shore. In order to resolve this ambiguity one must either employ more receivers or have a-priori knowledge sufficient to determine on which side of the receivers the source is located. This information would be used to aid in the selection of the initial conditions for ILS.

5. RESULTS

In this section we analyze the performance of the algorithms proposed in this paper in terms of their ability to characterize and localize a single LFMCW signal with structure identical to that of Signal 1 found in Table 2. We consider a single LFMCW signal in order to demonstrate performance that is free of any interactions

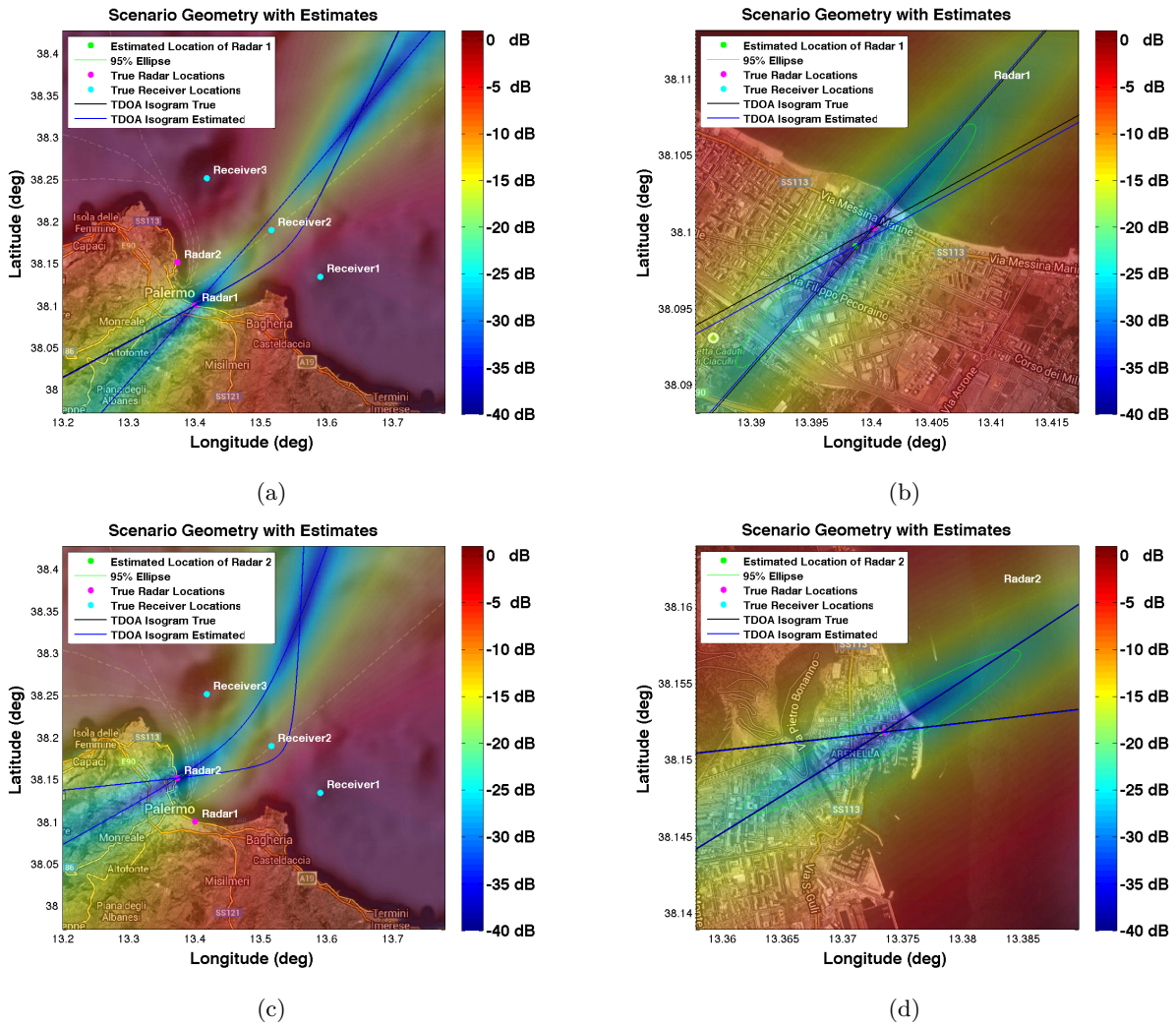


Figure 8: Localization Example Results

Table 7: Localization Results

	Miss Distance (m)	Semi-Major Axis Length (m)	Semi-Minor Axis Length (m)
Radar 1	185	1234	163
Radar 2	78	1182	160

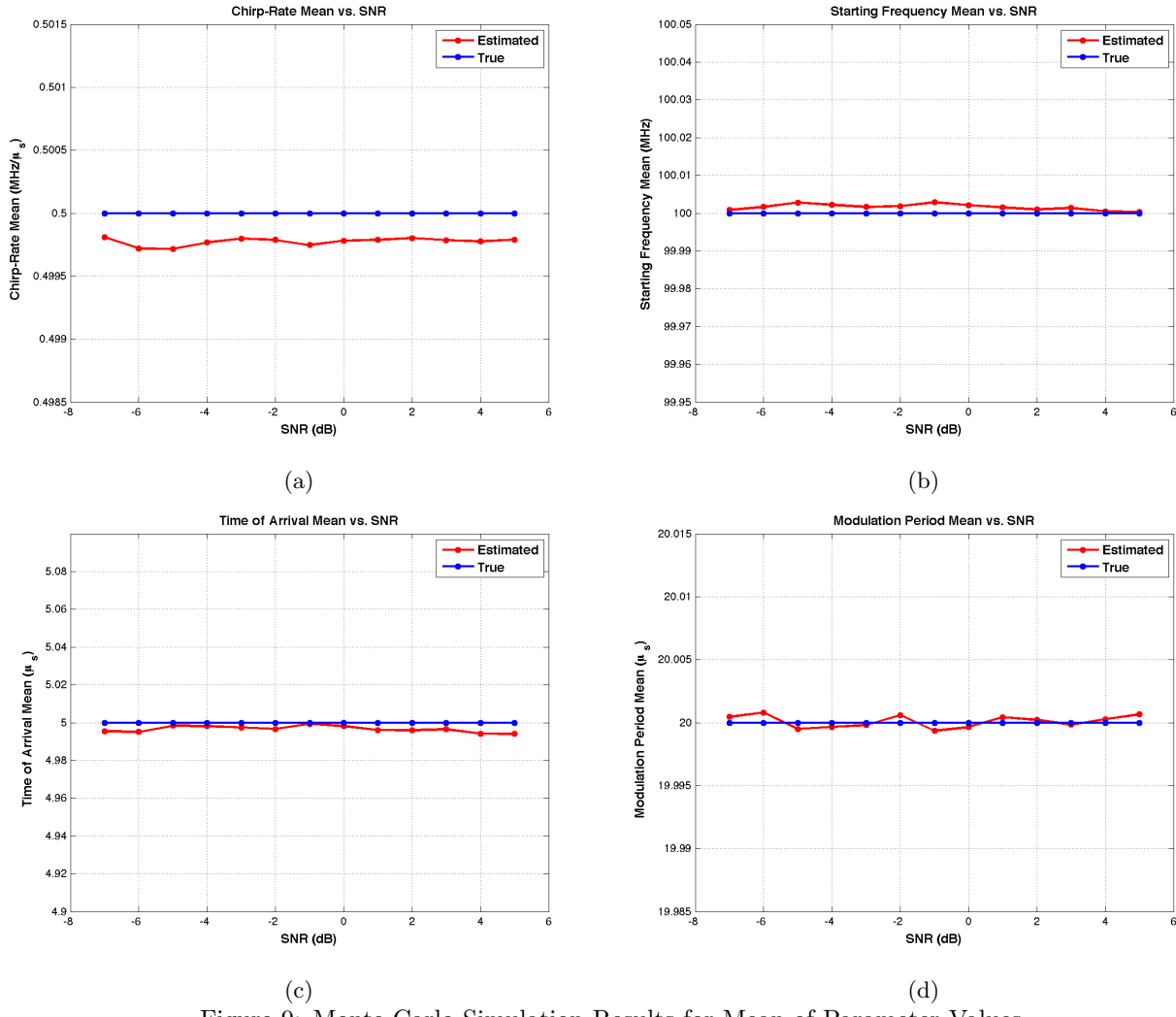


Figure 9: Monte Carlo Simulation Results for Mean of Parameter Values

that might result from a multi-signal environment. The reader is redirected to the simulation examples found in Sections 2, 3, and 4 for evidence supporting the success of the algorithms in multi-signal environments.

5.1 Characterization Monte Carlo Results

In this section we summarize the results of a 1000 trial Monte Carlo simulation for various levels of SNR. Figure 9 shows the true and estimated mean values taken over all trials for chirp-rate (Figure 9a), starting frequency (Figure 9b), TOA (Figure 9c), and modulation period (Figure 9d). Figures 9b, 9c and 9d indicate that the parameter estimates for starting frequency, TOA, and PRI are reasonably unbiased, while Figure 9a indicates that chirp-rate estimates are slightly biased. Determining the source and remedy for this problem is an area of future work. Figure 10 shows the estimated standard deviation computed over the same 1000 Monte Carlo trials. Figures 10a, 9b, 9c, and 10d indicate reasonably small estimation error variances that are roughly monotonically decreasing functions of SNR.

6. CONCLUSION

In this paper we developed an approach to Detecting, Characterizing, and Localizing multiple LPI LFMCW sources and demonstrated features of the approach that do not exist in any one approach that is known to the

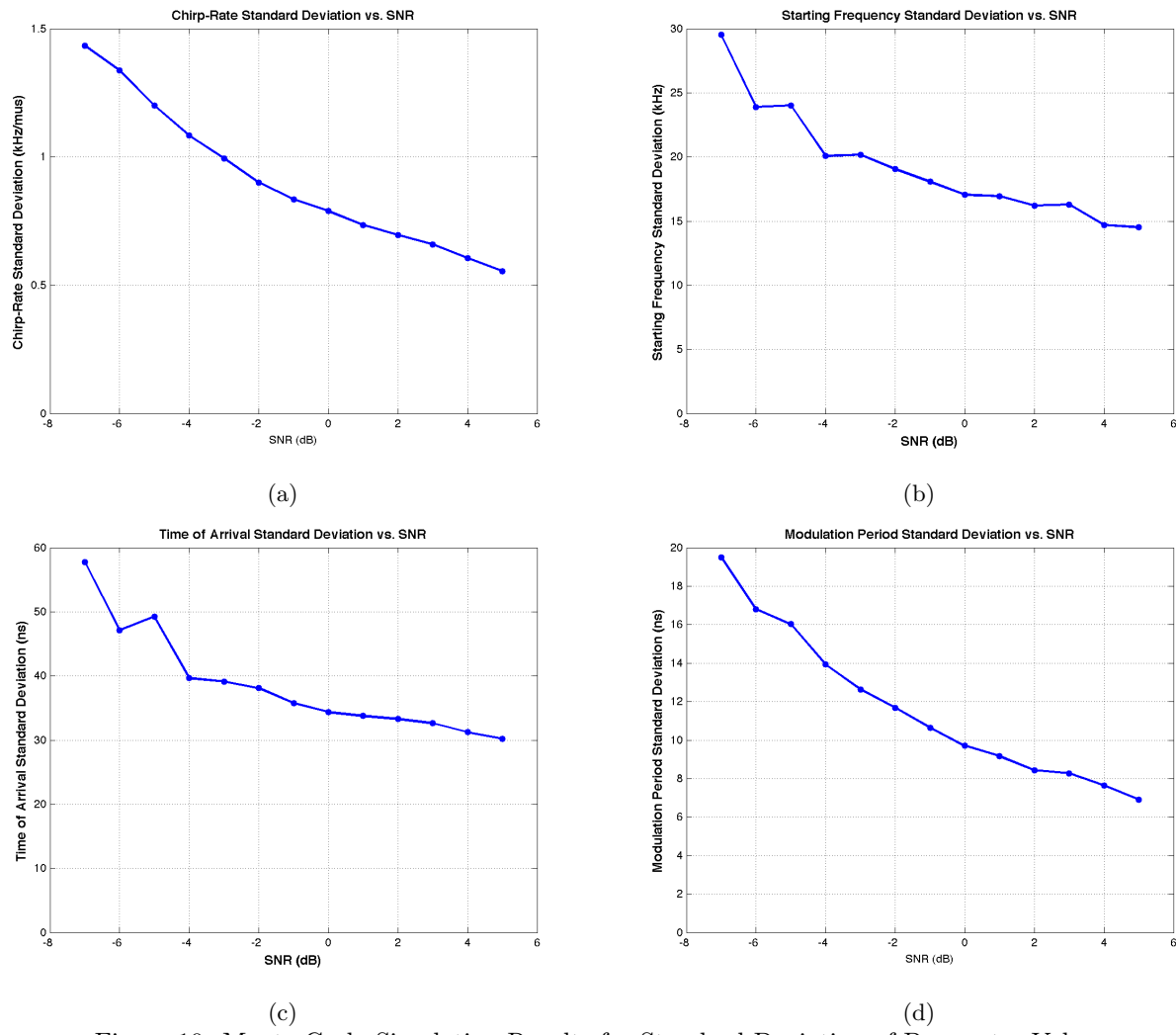


Figure 10: Monte Carlo Simulation Results for Standard Deviation of Parameter Values

authors in the literature and demonstrated its performance at a reasonably low SNR via simulation. In contrast to classical approaches to signal detection, such as is used to seeing in the literature,^{1,7} in large part our approach is *ad-hoc* up to the point where we initialize the MLE found in Equation (3). The upside to such an approach is that the virtuous aspects of methods from a wide variety of disciplines, such as signal processing,^{7,14} statistics,^{3,16} optimization,¹⁸ and optimal state estimation/geo-location,¹³ can be brought to bear on an old problem and yeild new fruit that is not only of theoretical interest, but also has promise for practical implementation.

REFERENCES

1. S. Kay and G. Boudreax-Bartels, "On the optimality of the wigner distribution for detection," in *Acoustics, Speech, and Signal Processing, IEEE International Conference on ICASSP'85.*, **10**, pp. 1017–1020, IEEE, 1985.
2. F. G. Geroleo and M. Brandt-Pearce, "Detection and estimation of lfmcw radar signals," *Aerospace and Electronic Systems, IEEE Transactions on* **48**(1), pp. 405–418, 2012.
3. D. B. Percival and A. T. Walden, *Spectral analysis for physical applications*, Cambridge University Press, 1993.
4. P. E. Pace, *Detecting and classifying low probability of intercept radar*, Artech House, 685 Canton Street, Norwood, MA 02062, 2nd ed., 2009.
5. R. G. Wiley, *ELINT: The interception and analysis of radar signals*, Artech House Boston, 2006.
6. M. A. Richards, *Fundamentals of radar signal processing*, Tata McGraw-Hill Education, 2005.
7. S. Kay, *Fundamentals of Statistical Signal Processing: Detection Theory*, vol. 2 of *Prentice Hall Signal Processing Series*, Prentice Hall, 1998.
8. L. Cohen, *Time-Frequency Analysis*, Prentice Hall Signal Processing Series, Prentice Hall, 1995.
9. P. Stoica and R. Moses, *Spectral analysis of signals*, Pearson/Prentice Hall, 2005.
10. J. S. Seybold, *Introduction to RF propagation*, Wiley, 2005.
11. D. Thomson, "Spectrum estimation and harmonic analysis," *Proceedings of the IEEE* **70**(9), pp. 1055–1096, 1982.
12. M. T. Grabbe, "A correlation algorithm for geo-location position measurements," 2011.
13. M. T. Grabbe, B. M. Hamschin, and A. P. Douglas, "A measurement correlation algorithm for line-of-bearing geo-location," in *Aerospace Conference, 2013 IEEE*, pp. 1–8, IEEE, March 2013.
14. S. Kay, *Fundamentals of Statistical Signal Processing: Estimation Theory*, vol. 1 of *Prentice Hall Signal Processing Series*, Prentice Hall, 1993.
15. J. Devore, *Probability and statistics for engineers and scientists*, CengageBrain.com, 4th ed., 2004.
16. W. T. V. William H. Press, Saul A. Teukolsky and B. P. Flannery, *Numerical Recipes in C: The art of scientific computing*, Cambridge university press, 2nd ed., 1988.
17. J. Wang, W. W. Tsang, and G. Marsaglia, "Evaluating kolmogorov's distribution," *Journal of Statistical Software* **8**(18), 2003.
18. J. H. Mathews and K. D. Fink, *Numerical methods using MATLAB*, vol. 31, Prentice hall Upper Saddle River, NJ, 3rd ed., 1999.
19. A. Oppenheim, R. Schafer, and J. Buck, *Discrete-Time Signal Processing*, Prentice Hall, 1999.
20. S. Stein, "Algorithms for ambiguity function processing," *Acoustics, Speech and Signal Processing, IEEE Transactions on* **29**(3), pp. 588–599, 1981.
21. M. T. Grabbe and B. M. Hamschin, "Time difference of arrival estimation for pulsed signals," Memo KVW-0-12-U-001, The Johns Hopkins University Applied Physics Laboratory, Laurel, MD, February 2012.
22. Y. Bar-Shalom, P. K. Willett, and X. Tian, *Tracking and Data Fusion: A Handbook of Algorithms*, YBS Publishing, 2011.
23. B. Decker, "World geodetic system 1984," tech. rep., DTIC Document, 1986.
24. M. T. Grabbe and B. M. Hamschin, *Passive Emitter Geo-Location: Measurements and Algorithms*. The Johns Hopkins University Applied Physics Lab, 11100 Johns Hopkins Rd, Laurel, MD, 20723-6099, 1st ed., September 2012.
25. D. Luenberger and Y. Ye, *Linear and nonlinear programming*, Springer Verlag, 2008.
26. M. T. Grabbe, "A numerical method for constructing geo-location isograms," June 2011.